JAN 2 3 1995

Y3 N33:35/5063

NUREG/CR-5063
MEA-2268

Development of a Mechanistic Understanding of Radiation Embrittlement in Reactor Pressure Vessel Steels

Final Report

Prepared by F. Ebrahimi, D. T. Hoelzer, D. Venables, and V. Krishnamoorthy

University of Fiorida

Materials Engineering Associates, Inc.

Prepared for
U.S. Nuclear Regulatory
Commission

COMPLETED

BEST COPY AVAILABLE ORIGINAL

NOTICE

This report was prepared as an account of work sponsored by an agency of the United States Government. Neither the United States Government nor any agency thereof, or any of their employees, makes any warranty, expressed or implied, or assumes any legal liability of responsibility for any third party's use, or the results of such use, of any information, apparatus, product or process disclosed in this report, or represents that its use by such third party would not infringe privately owned rights.

NOTICE

Availability of Reference Materials Cited in NRC Publications

Most documents cited in NRC publications will be available from one of the following sources:

1. The NRC Public Document Room, 1717 H Street, N.W.
Washington, DC 20555
2. The Superintendent of Documents, U.S. Government Printing Office, Post Office Box 37082,
Washington, DC 20013-7082
3. The National Technical Information Service, Springfield, VA 22161

Although the listing that follows represents the majority of documents cited in NRC publications, it is not intended to be exhaustive.

Referenced documents available for inspection and copying for a fee from the NRC Public Document Room include NRC correspondence and internal NRC memoranda; NRC Office of Inspection and Enforcement bulletins, circulars, information notices, inspection and investigation notices; Licensee Event Reports; vendor reports and correspondence; Commission papers; and applicant and licensee documents and correspondence.

The following documents in the NUREG series are available for purchase from the GPO Sales Program: formal NRC staff and contractor reports, NRC-sponsored conference proceedings, and NRC booklets and brochures. Also available are Regulatory Guides, NRC regulations in the *Code of Federal Regulations*, and *Nuclear Regulatory Commission Issuances*.

Documents available from the National Technical Information Service include NUREG-series reports and technical reports prepared by other federal agencies and reports prepared by the Atomic Energy Commission, forerunner agency to the Nuclear Regulatory Commission.

Documents available from public and special technical libraries include all open literature items, such as books, journal and periodical articles, and transactions. *Federal Register* notices, federal and state legislation, and congressional reports can usually be obtained from these libraries.

Documents such as theses, dissertations, foreign reports and translations, and non-NRC conference proceedings are available for purchase from the organization sponsoring the publication cited.

Single copies of NRC draft reports are available free, to the extent of supply, upon written request to the Division of Information Support Services, Distribution Section, U.S. Nuclear Regulatory Commission, Washington, DC 20555.

Copies of industry codes and standards used in a substantive manner in the NRC regulatory process are maintained at the NRC Library, 7920 Norfolk Avenue, Bethesda, Maryland, and are available there for reference use by the public. Codes and standards are usually copyrighted and may be purchased from the originating organization or, if they are American National Standards, from the American National Standards Institute, 1430 Broadway, New York, NY 10018.

NUREG/CR-5063
MEA-2268
RF, R5

Development of a Mechanistic Understanding of Radiation Embrittlement in Reactor Pressure Vessel Steels

Final Report

Manuscript Completed: December 1987
Date Published: January 1988

Prepared by
F. Ebrahimi, D. T. Hoelzer, D. Venables, and V. Krishnamoorthy

Department of Materials Science and Engineering
University of Florida
Gainesville, FL 32611

Under Contract to:
Materials Engineering Associates, Inc.
9700-B Martin Luther King, Jr. Highway
Lanham, MD 20706-1837

Prepared for
Division of Engineering
Office of Nuclear Regulatory Research
U.S. Nuclear Regulatory Commission
Washington, DC 20555
NRC FIN B8900

II

ABSTRACT

The microstructures of a series of reactor pressure vessel (RPV) steels and model iron alloys with various copper, nickel, and phosphorus contents were examined in the unirradiated condition and neutron-irradiated (fluence of 2 to 4.63 x 10^{19} n/cm^2, E > 1 MeV at ~ 288°C) conditions using high resolution analytical microscopy techniques to understand the mechanisms by which these elements affect the radiation embrittlement sensitivity of RPV steels. Fractography techniques were employed to identify embrittlement mechanisms that would be manifested as a change in the fracture surface properties.

Analysis showed that radiation hardening in the reference iron alloy is associated with the formation of prismatic dislocation loops of an interstitial nature with mainly a<100> Burgers vector. The absence of significant radiation hardening reported for the low Cu-low P steel alloy was found to be consistent with the very low density of dislocation loops with mainly a/2<111> Burgers vector.

Copper was found to decrease the size and to increase the number density of observable defects. However, the enhancement of radiation embrittlement sensitivity in copper-containing alloys is due to the radiation-enhanced formation of Cu-rich clusters/precipitates. The slight reduction in the radiation hardening of iron by a nickel addition is attributed to a modification of the defect structure. No synergism between copper and nickel was found in the model iron alloys, except for an enrichment of copper clusters with nickel.

In both irradiated and unirradiated high P steels, phosphorus had segregated to particle/matrix interfaces, which is consistent with the reported lower upper-shelf energies of high P alloys. The fracture surface was transgranular for these steels and no intergranular fracture was observed. Phosphorus also decreased the radiation-induced defect size significantly. However, the detrimental effect of phosphorus on radiation embrittlement sensitivity in the absence of copper is attributed to the radiation-induced clustering of phosphorus. The absence of phosphorus clusters in the high Cu-high P model iron alloy may explain the inactive role of phosphorus in radiation embrittlement sensitivity of RPV steels in the presence of copper.

The effect of alloying/impurity elements on the evolution of defect structures during neutron irradiation is ascribed to vacancy trapping by solute atoms, which results in survival of a/2<111> loops. Consequently, the number density of defects is increased while the size and the total area of the dislocation loops are reduced.

BLANK PAGE

CONTENTS

	Page
ABSTRACT	iii
LIST OF FIGURES	vii
LIST OF TABLES	ix
FOREWORD	xi
ACKNOWLEDGMENT	xv
1. INTRODUCTION	1
2. MATERIALS AND EXPERIMENTAL PROCEDURES	6
2.1 Materials	6
2.2 Experimental Procedures	7
2.2.1 Experimental Procedures for Scanning Electron Microscopy	7
2.2.2 Experimental Procedures for Transmission Electron Microscopy	8
2.2.3 Experimental Procedures for Field Ion Microscopy/Atom Probe	8
2.2.4 Experimental Procedures for Auger Electron Spectroscopy	9
3. MICROSTRUCTURAL CHARACTERIZATION	10
3.1 Unirradiated Materials	10
3.1.1 Iron Alloys	10
3.1.2 Steel Alloys	13
3.2 Irradiated Materials	13
3.2.1 Iron Alloys	13
3.2.2 Steel Alloys	36
3.3 Thermally Aged Iron Alloys	40
4. FRACTOGRAPHY AND THE FRACTURE SURFACE ANALYSIS	48
5. THE CORRELATION BETWEEN MICROSTRUCTURE AND RADIATION HARDENING	56
6. COMMENTS ON RADIATION EMBRITTLEMENT OF RPV STEELS	62
7. SUMMARY	63
REFERENCES	66
APPENDIX A	

BLANK PAGE

LIST OF FIGURES

Figure		Page
1	Schematic representation of CVN impact energy vs. temperature illustrating radiation damage embrittlement	2
2	TEM micrographs showing the precipitate microstructures of unirradiated reference iron and Fe-0.3Cu alloys	11
3	TEM micrograph showing ε-carbide platelets	12
4	TEM micrographs showing the general microstructure of the steel alloys before irradiation	14
5	TEM micrograph showing the defect structure in the irradiated reference iron alloy	16
6	TEM micrograph showing the defect structure in the irradiated Fe-0.3Cu iron alloy	17
7	TEM micrograph showing the defect structure in the irradiated Fe-0.7Ni iron alloy	18
8	TEM micrograph showing the defect structure in the irradiated Fe-0.4Ni-0.3Cu iron alloy	19
9	TEM micrograph showing the defect structure in the irradiated Fe-0.7Ni-0.3Cu iron alloy	20
10	TEM micrograph showing the defect structure in the irradiated Fe-0.7Ni-0.025P iron alloy	21
11	TEM micrograph showing the defect structure in the irradiated Fe-0.7Ni-0.3Cu-0.025P alloy under weak beam condition	22
12	TEM micrographs showing denuded zones of defects in the irradiated reference iron alloy	24
13	TEM micrographs showing the formation of large dislocation loops adjacent to dislocations	25
14	TEM micrographs showing the typical distribution of in-matrix cementite particles	29
15	TEM micrograph showing the precipitation of α"-nitrides in the matrix and on a dislocation	31
16	TEM micrographs showing the precipitates in bulk-irradiated Fe-0.7Ni-0.025P alloy	32
17	TEM micrograph showing α"-nitride precipitates on a carbide/matrix interface	33

LIST OF FIGURES

Figure		Page
18	TEM micrographs showing the absence of nitride precipitates on dislocations and demonstrating the foil thickness effect	34
19	TEM micrographs showing the general microstructural features in the irradiated steel alloys	37
20	TEM micrograph showing the sparsely distributed large dislocation loops in irradiated steel alloys	38
21	TEM micrograph showing the fine needle-like precipitates found in the irradiated high P-low Cu steel alloy	39
22	TEM micrographs showing the dissolution of cementite particles in the reference iron alloy after long time aging at 288°C	41
23	TEM micrographs comparing the amount of cementite particles left in the matrix after thermal aging	42
24	TEM micrographs showing the image contrast of α"-nitrides formed on a dislocation under dynamical two-beam condition	44
25	TEM micrographs showing the image contrast of α"-nitrides formed on a cementite particle under two-beam condition	45
26	TEM micrographs showing formation of α"-nitride in furnace-cooled iron alloy sample and absence of nitrides in air-cooled iron alloy sample	46
27	TEM micrographs showing formation of α"-nitrides on precipitates formed on periphery of cementite ghost	47
28	SEM fractographs showing the transgranular cleavage morphology of brittle fracture in unirradiated and irradiated high P-low Cu steel alloy	49
29	SEM fractographs showing the shear zone adjacent to the V-notch in irradiated high P-low Cu steel	50
30	SEM fractograph and extraction replica TEM micrograph from fracture surface of irradiated specimen	51
31	Auger spectrum from the surface of a particle showing phosphorus accumulation at the interface	52
32	Auger spectrum showing the accumulation of phosphorus on an oxide particle and SEM micrograph	53

LIST OF TABLES

Table		Page
1	A General Approach to Investigate the Effect of Composition on Radiation Embrittlement in Reactor Pressure Vessel Steels	4
2	Chemical Compositions of Steel Alloys	6
3	Chemical Compositions of Iron Alloys	7
4	Results of Quantitative Analysis of Observable Dislocation Loops in Irradiated Iron Alloys	15
5	Theoretical Predictions of Strengthening by Irradiation-Induced Aggregates in Iron Alloys	59
6	Theoretical Predictions of Strengthening by Irradiation-Induced Aggregates in Steel Alloys	60

BLANK PAGE

FOREWORD

The work reported here was performed at Materials Engineering Associates (MEA) under the program Structural Integrity of Water Reactor Pressure Boundary Components, F. J. Loss, Program Manager. The program is sponsored by the Office of Nuclear Regulatory Research of the U. S. Nuclear Regulatory Commission (NRC). The technical monitor for the NRC is Alfred Taboada.

Prior reports under the current contract are listed below:

1. J. R. Hawthorne, "Significance of Nickel and Copper to Radiation Sensitivity and Postirradiation Heat Treatment Recovery of Reactor Vessel Steels," USNRC Report NUREG/CR-2948, Nov. 1982.

2. "Structural Integrity of Water Reactor Pressure Boundary Components, Annual Report for 1982," F. J. Loss, Ed., USNRC Report NUREG/CR-3228, Vol. 1, Apr. 1983.

3. J. R. Hawthorne, "Exploratory Assessment of Postirradiation Heat Treatment Variables in Notch Ductility Recovery of A 533-B Steel," USNRC Report NUREG/CR-3229, Apr. 1983.

4. W. H. Cullen, K. Torronen, and M. Kemppainen, "Effects of Temperature on Fatigue Crack Growth of A 508-2 Steel in LWR Environment," USNRC Report NUREG/CR-3230, Apr. 1983.

5. "Proceedings of the International Atomic Energy Agency Specialists' Meeting on Subcritical Crack Growth," Vols. 1 and 2, W. H. Cullen, Ed., USNRC Conference Proceeding NUREG/CP-0044, May 1983.

6. W. H. Cullen, "Fatigue Crack Growth Rates of A 508-2 Steel in Pressurized, High-Temperature Water," USNRC Report NUREG/CR-3294, June 1983.

7. J. R. Hawthorne, B. H. Menke, and A. L. Hiser, "Notch Ductility and Fracture Toughness Degradation of A 302-B and A 533-B Reference Plates from PSF Simulated Surveillance and Through-Wall Irradiation Capsules," USNRC Report NUREG/CR-3295, Vol. 1, Apr. 1984.

8. J. R. Hawthorne and B. H. Menke, "Postirradiation Notch Ductility and Tensile Strength Determinations for PSF Simulated Surveillance and Through-Wall Specimen Capsules," USNRC Report NUREG/CR-3295, Vol. 2, Apr. 1984.

9. A. L. Hiser and F. J. Loss, "Alternative Procedures for J-R Curve Determination," USNRC Report NUREG/CR-3402, July 1983.

10. A. L. Hiser, F. J. Loss, and B. H. Menke, "J-R Curve Characterization of Irradiated Low Upper Shelf Welds," USNRC Report NUREG/CR-3506, Apr. 1984.

11. W. H. Cullen, R. E. Taylor, K. Torronen, and M. Kemppainen, "The Temperature Dependence of Fatigue Crack Growth Rates of A 351 CF8A Cast Stainless Steel in LWR Environment," USNRC Report NUREG/CR-3546, Apr. 1984.

12. "Structural Integrity of Light Water Reactor Pressure Boundary Components -- Four-Year Plan 1984-1988," F. J. Loss, Ed., USNRC Report NUREG/CR-3788, Sep. 1984.

13. W. H. Cullen and A. L. Hiser, "Behavior of Subcritical and Slow-Stable Crack Growth Following a Postirradiation Thermal Anneal Cycle," USNRC Report NUREG/CR-3833, Aug. 1984.

14. "Structural Integrity of Water Reactor Pressure Boundary Components: Annual Report for 1983," F. J. Loss, Ed., USNRC Report NUREG/CR-3228, Vol. 2, Sept. 1984.

15. W. H. Cullen, "Fatigue Crack Growth Rates of Low-Carbon and Stainless Piping Steels in PWR Environment," USNRC Report NUREG/CR-3945, Feb. 1985.

16. W. H. Cullen, M. Kemppainen, H. Hanninen, and K. Torronen, "The Effects of Sulfur Chemistry and Flow Rate on Fatigue Crack Growth Rates in LWR Environments," USNRC Report NUREG/CR-4121, Feb. 1985.

17. "Structural Integrity of Water Reactor Pressure Boundary Components: Annual Report for 1984," F. J. Loss, Ed., USNRC Report NUREG/CR-3228, Vol. 3, June 1985.

18. A. L. Hiser, "Correlation of C_v and K_{Ic}/K_{Jc} Transition Temperature Increases Due to Irradiation," USNRC Report NUREG/CR-4395, Nov. 1985.

19. W. H. Cullen, G. Gabetta, and H. Hanninen, "A Review of the Models and Mechanisms For Environmentally-Assisted Crack Growth of Pressure Vessel and Piping Steels in PWR Environments," USNRC Report NUREG/CR-4422, Dec. 1985.

20. "Proceedings of the Second International Atomic Energy Agency Specialists' Meeting on Subcritical Crack Growth," W. H. Cullen, Ed., USNRC Conference Proceeding NUREG/CP-0067, Vols. 1 and 2, Apr. 1986.

21. J. R. Hawthorne, "Exploratory Studies of Element Interactions and Composition Dependencies in Radiation Sensitivity Development," USNRC Report NUREG/CR-4437, Nov. 1985.

22. R. B. Stonesifer and E. F. Rybicki, "Development of Models for Warm Prestressing," USNRC Report NUREG/CR-4491, Jan. 1987.

23. E. F. Rybicki and R. B. Stonesifer, "Computational Model for Residual Stresses in a Clad Plate and Clad Fracture Specimens," USNRC Report NUREG/CR-4635, Oct. 1986.

24. D. E. McCabe, "Plan for Experimental Characterization of Vessel Steel After Irradiation," USNRC Report NUREG/CR-4636, Oct. 1986.

25. E. F. Rybicki, J. R. Shadley, and A. S. Sandhu, "Experimental Evaluation of Residual Stresses in a Weld Clad Plate and Clad Test Specimens," USNRC Report NUREG/CR-4646, Oct. 1986.

26. "Structural Integrity of Water Reactor Pressure Boundary Components: Annual Report for 1985," F. J. Loss, Ed., USNRC Report NUREG/CR-3228, Vol. 4, June 1986.

27. G. Gabetta and W. H. Cullen, "Application of a Two-Mechanism Model for Environmentally-Assisted Crack Growth," USNRC Report NUREG/CR-4723, Oct. 1986.

28. W. H. Cullen, "Fatigue Crack Growth Rates in Pressure Vessel and Piping Steels in LWR Environments," USNRC Report NUREG/CR-4724, Mar. 1987.

29. W. H. Cullen, M. E. Mayfield, and M. R. Jolles, "Fatigue Crack Growth of Part-Through Cracks in Pressure Vessel and Piping Steels: Air Environment Results, USNRC Report NUREG/CR-4828 (in publication).

30. D. E. McCabe, "Evaluation of Surface Cracks Embedded in Reactor Vessel Cladding Unirradiated Bend Specimens," USNRC Report NUREG/CR-4841, May 1987.

31. H. Hanninen, M. Vulli, and W. H. Cullen, "Surface Spectroscopy of Pressure Vessel Steel Fatigue Fracture Surface Films Formed in PWR Environments," USNRC Report NUREG/CR-4863, July 1987.

32. A. L. Hiser and G. M. Callahan, "A User's Guide to the NRC's Piping Fracture Mechanics Data Base (PIFRAC)," USNRC Report NUREG/CR-4894, May 1987.

33. "Proceedings of the Second CSNI Workshop on Ductile Fracture Test Methods (Paris, France, April 17-19, 1985)," F. J. Loss, Ed., USNRC Conference Proceeding NUREG/CP-0064, (in publication).

34. W. H. Cullen and D. Broek, "The Effects of Variable Amplitude Loading on A 533-B Steel in High-Temperature Air and Reactor Water Environments," USNRC Report NUREG/CR-4929 (in publication).

35. "Structural Integrity of Water Reactor Pressure Boundary Components: Annual Report for 1986," F. J. Loss, Ed., USNRC Report NUREG/CR-3228, Vol. 5, July 1987.

Prior reports[a] dealing with the specific topic of this report are listed below:

F. Ebrahimi and J. Hren, "Development of a Mechanistic Understanding of Radiation Embrittlement in Reactor Pressure Vessel Steels," Interim Report No. 1, University of Florida, Gainesville, FL, Oct. 1985.

D. T. Hoelzer and F. Ebrahimi, "Development of Reference Properties: Iron Alloys Microstructure," Interim Report No. 2, University of Florida, Gainesville, FL, May 1986.

D. Venables, D. T. Hoelzer, and F. Ebrahimi, "Preliminary Model Development: Phosphorus Effect," Interim Report No. 3, University of Florida, Gainesville, FL, Oct. 1986.

F. Ebrahimi and D. T. Hoelzer, "Preliminary Model Development: Copper and Nickel Effects," Interim Report No. 4, University of Florida, Gainesville, FL, June 1987.

---

[a] These reports are available at the Library and Department of Materials Science and Engineering of the University of Florida, Gainesville, FL

ACKNOWLEDGMENT

This is the Final Report of a three-year research program entitled "Development of a Mechanistic Understanding of Radiation Embrittlement in Reactor Pressure Vessel Steels," undertaken by the Department of Materials Science and Engineering at the University of Florida. This report summarizes the results in the previous four Interim Reports. New findings since the Interim Report No. 4, June 1987, are included. Finally, a discussion of the mechanisms by which copper, nickel, and phosphorus influence the radiation embrittlement sensitivity of RPV steels is presented.

This research program was sponsored by the Nuclear Regulatory Commission through Materials Engineering Associates, Inc., Lanham, MD, under Contract No. 83092302 with the University of Florida. Dr. F. Ebrahimi, Assistant Professor, is the Principal Investigator, and D. T. Hoelzer, D. Venables, and V. Krishnamoorthy are graduate students in the Department of Materials Science and Engineering at the University of Florida. The Program Monitor of this project is J. R. Hawthorne. Contributions from Dr. J. Hren, Dr. S. D. Walck, and Dr. J. Newkirk are greatly appreciated.

Special gratitude is due to the Oak Ridge National Laboratory for use of their high resolution analytical TEM facilities for the compositional analysis of carbides and the FIM/AP facilities for the analysis of ultrafine precipitates/clusters. Contributions from Dr. P. Maziasz and Dr. M. Miller at ORNL are gratefully acknowledged. Their efforts were sponsored by the Division of Materials Sciences, U. S. Department of Energy, under Contract No. DE-AC05-840R21400 with Martin Marietta Energy Systems, Inc. and through the ShaRE Program under Contract No. DE-AC05-760R00033 with Oak Ridge Associated Universities.

We wish to thank the Department of Nuclear Sciences at the University of Florida for providing the storage area for radioactive materials and a shielded work area for cutting and handling radioactive specimens. Special thanks are due to Dr. W. G. Vernetson, Mr. D. Munroe, and Mr. C. J. Stiehl for their invaluable help.

1. INTRODUCTION

Water reactor pressure vessels (RPV's) operate at a nominal temperature of ~ 288°C and are subjected to neutron irradiation. This irradiation service results in an increase in the ductile-to-brittle transition temperature and a decrease in upper-shelf energy absorption as determined by Charpy V-notch (C_v) impact testing (Ref. 1) (Fig. 1). Older RPV's were constructed from A 302-B and A 533-B steels and weldments, which contain traces of impurity elements such as copper and phosphorus. The presence of certain impurity/alloying elements in RPV steels has been found to enhance irradiation embrittlement sensitivity at ~ 288°C. Among these elements, copper, phosphorus, and nickel have been shown to have a most significant effect (Ref. 2).

The increase in ductile-to-brittle transition temperature associated with the irradiation embrittlement of RPV steels has been attributed to radiation hardening (Refs. 2-4). A linear relationship between the shift in the ductile-to-brittle transition temperature and the increase in yield strength has been proposed (Ref. 4). Although this empirical model is capable of explaining the reduction of resistance to brittle fracture due to the elevation of yield strength, it fails to predict the decrease in upper-shelf energy (see Appendix A). A consideration of the reduction in strain-hardening capacity due to irradiation is required to account for the loss in resistance to ductile crack initiation and propagation. In general, the fracture process associated with C_v testing is complex (Ref. 5), and many parameters should be considered in interpreting C_v energy data.

The increase in yield strength and the loss of strain-hardening capacity of ferritic alloys have been attributed to the creation of defects or defect clusters by the neutron bombardment, which restrict the movement of glide dislocations (Ref. 6). The point defects (interstitials and vacancies) generated in the displacement cascades during neutron irradiation can (1) recombine, (2) be trapped by impurity atoms, (3) cluster and collapse to dislocation loops, (4) coalesce (vacancies) and form voids, and/or (5) migrate to sinks such as interfaces and dislocations. The migration of point defects towards the sinks may result in radiation-induced segregation and radiation-enhanced diffusion, both of which can cause radiation-induced precipitation in alloys (Ref. 7). In ferritic iron alloys, the type and the extent of microstructural damage depends on (a) the irradiation parameters, i.e., irradiation temperature, neutron fluence rate, and total neutron fluence, (b) the chemical composition, and (c) the preirradiation microstructure.

The deleterious effect of Cu on radiation embrittlement sensitivity has been attributed to an enhancement of radiation hardening. It has been suggested by many investigators (Refs. 8-14), using Transmission Electron Microscopy (TEM), Field Ion Microscopy/Atom Probe (FIM/AP), and Small Angle Neutron Scattering (SANS) techniques, that Cu increases the radiation hardening sensitivity by two mechanisms:

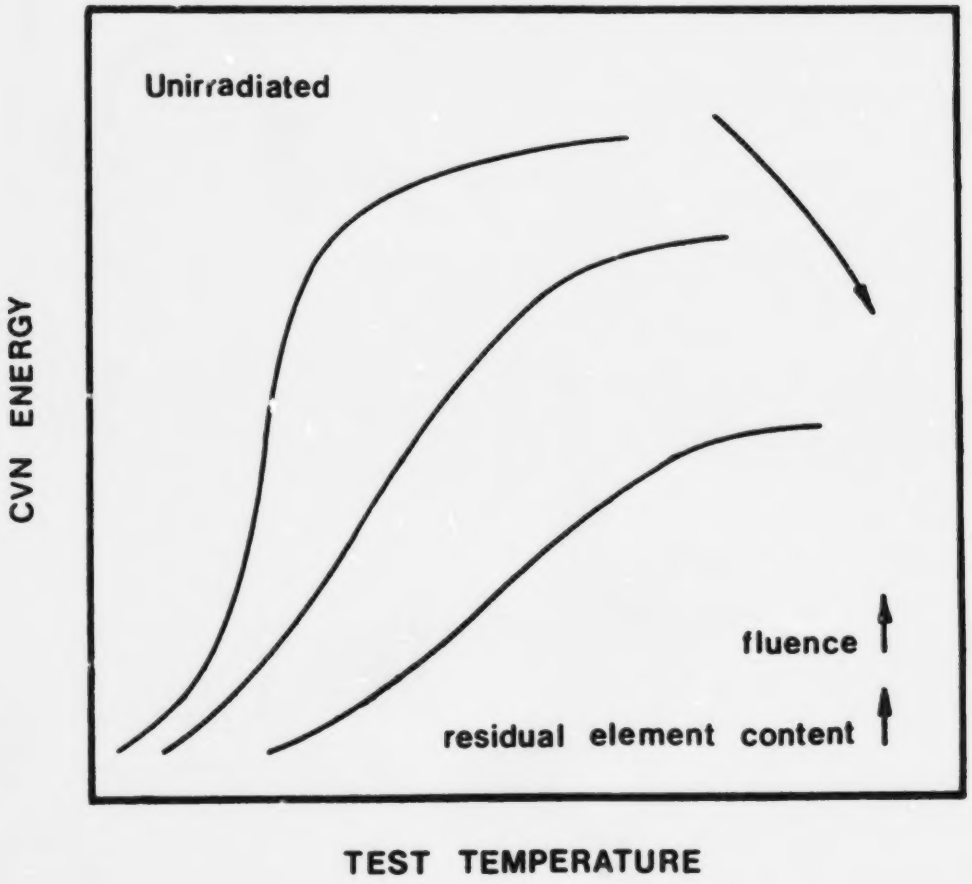

Fig. 1 Schematic representation of C_v impact energy vs. temperature illustrating radiation-induced embrittlement.

BEST COPY AVAILABLE

(1) an increase in the density accompanied by a decrease in the size of radiation defects (dislocation loops and voids) and (2) radiation-induced precipitation. The latter mechanism has been attributed to a diffusion-enhanced precipitation (Refs. 13-15); the former mechanism has been suggested to be due to an enhanced nucleation of radiation defects (Refs. 8, 9, and 13). For a given composition, the relative contribution of each mechanism to strengthening is expected to depend on the irradiation temperature, the neutron fluence rate, and the preirradiation microstructure, all of which contribute significantly to the dislocation evolution during neutron irradiation (Refs. 16-17). The effect of Cu on the irradiation embrittlement of RPV steels has been reported to be enhanced by the addition of nickel above a minimum copper content level (Refs. 18-19). Although the synergism between copper and nickel has been established, the mechanism by which nickel enhances the detrimental effect of Cu is not known. Recent results (Ref. 20) indicate an increase in the yield strength, paralleling the increase in ductile-to-brittle transition temperature of RPV steels due to additions of nickel in copper-containing steels.

In contrast to the large number of studies on the effect of copper, no systematic evaluation of the mechanisms by which phosphorus affects the radiation embrittlement sensitivity has been performed. Recent results (Ref. 20) reveal that the addition of phosphorus to low copper steels increases the radiation embrittlement sensitivity of RPV steels and that the detrimental effect of phosphorus is manifested as an increase in the radiation hardening. On the other hand, additions of phosphorus in the presence of copper seem to have no significant effect on either the ductile-to-brittle transition temperature or the yield strength.

The purpose of this program was to study the mechanisms whereby Cu and P individually enhance the radiation sensitivity of RPV steels, and to investigate the interactions between copper and nickel, and between copper and phosphorus in radiation embrittlement sensitivity development. Both pressure vessel steels and model iron alloys with various amounts of Cu, P and Ni were studied. The iron and steel alloys studied were prepared, irradiated, and mechanically tested by Materials Engineering Associates (MEA). The main role of the research group at the University of Florida was to characterize the microstructure of the alloys using high resolution analytical microscopy techniques and to develop mechanistic models for the effects of Cu, P, and Ni explaining the evolution of microstructure during neutron irradiation. Table 1 shows our general approach to investigate radiation embrittlement in RPV steels.

The results of our efforts during the three year duration of this program were previously reported in the form of four Interim Reports (Refs. 21-24). This Final Report summarizes the results previously documented and includes new determinations since our last Interim Report (Ref. 24). The materials studied and a brief description of the experimental procedures are presented in Section 2. Section 3 is devoted to the results and discussion of microstructural characterizations of the steel and model iron alloys in unirradiated, irradiated,

Table 1 A General Approach to Investigate the Effect of Composition on Radiation Embrittlement in Reactor Pressure Vessel Steels

	Phenomena	Embrittlement Mechanisms	Experimental Observations[a]	Elements
I.	Radiation-enhanced segregation to prior austenite boundaries	• Cohesive strength at boundaries ↓ • σ_F ↓	• Intergranular fracture (SEM)	• P
II.	Radiation-enhanced segregation to carbide/matrix interfaces	• Cohesive strength at interfaces ↓ • Microvoid initiation strain ↓ • Fracture strain • σ_F ↓	• Shallow microvoids (SEM) • Surface analysis (AES/SAM)	• P
III.	Modification of radiation-enhanced and/or induced changes in carbide microstructure (dissolution, ripening, reprecipitation)	• Fracture stress • Fracture strain ↓ • $\sigma - \varepsilon$	• Size, density, and composition of carbides (TEM) • Size of microvoids (SEM) • Size of carbides associated with microvoids (TEM, extraction replica)	• P, Cu?
IV.	Modification of radiation-induced defects • Dislocation loops • Voids • Complexes	• $\sigma - \varepsilon$ relationship • Yield strength ↑ • Strain-hardening capacity ↓ • Fracture strain ↓	• Density, size and distribution of dislocation loops (TEM) • Voids (TEM, FIM/AP)	• P, Cu, Ni
V.	Radiation-induced and/or enhanced clustering or precipitation	• $\sigma - \varepsilon$ relationship • Yield strength ↑ • Strain-hardening capacity ↓ • Fracture strain ↓	• Existence of clusters or precipitates (TEM, FIM/AP/IAP)	• P, Cu, Ni

[a] Based on the facilities available to the authors at the University of Florida

and thermally aged conditions. The results of fractography and Auger Electron Spectroscopy/Scanning Auger Microscopy (AES/SAM) analyses of the steel alloys are given in Section 4. The mechanisms whereby Cu, P, and Ni affect radiation hardening of model iron alloys are discussed in Section 5. Comments are made on connections between (1) microstructure, (2) radiation hardening, and (3) irradiation embrittlement in Section 6. Finally, the results of this program are summarized in Section 7.

2. MATERIALS AND EXPERIMENTAL PROCEDURES

2.1 Materials

The materials studied in this program were prepared and irradiated by MEA. The chemical compositions of the steel alloys examined in this investigation and their designated codes are given in Table 2. These steels are part of a larger materials matrix designed by MEA for obtaining statistical combinations of specific impurities and/or alloying elements with primary base compositions of A 302-B and A 533-B pressure vessel steels. C_v specimens of each steel were irradiated at a controlled temperature of 288°C (target) to a neutron fluence of $\sim 2 \times 10^{19}$ n/cm^2 (E > 1 MeV). The irradiated and unirradiated steel samples provided to the University of Florida were in the form of broken C_v specimens. For further information on the heat treatment and irradiation condition, the reader is directed to Reference 25.

Table 2 Chemical Compositions of Steel Alloys (A 302-B)[a]

Code	Composition (Wt %)								
	C	Mn	P	S	Si	Cu	Ni	Mo	N
67A	0.23	1.31	0.003	0.018	0.20	0.002	0.70	0.51	0.009
67B	0.23	1.31	0.015	0.018	0.20	0.002	0.70	0.51	0.009
67C	0.23	1.31	0.025	0.018	0.20	0.002	0.70	0.51	0.009
68A	0.23	1.31	0.003	0.017	0.22	0.30	0.70	0.52	0.010
68B	0.23	1.31	0.016	0.017	0.22	0.30	0.70	0.52	0.010
68C	0.23	1.31	0.028	0.017	0.22	0.30	0.70	0.52	0.010

[a] Hot rolled to 15-mm gage
Heat treatment: 900°C, 1 h, air cool
649°C, 1 h, water quench
677°C, 5 h, water quench
Microstructure: Tempered upper bainite and proeutectoid ferrite
Irradiation parameters: Specimen: Charpy V-notch
Hours of exposure: 740-750
Temperature: ~ 288°C
Average fluence: $\sim 2.5 \times 10^{19}$ n/cm^2, E > 1 MeV

The model iron alloys were designed to illuminate the roles of Cu, Ni, and P in radiation sensitivity development. The base material used for melting iron alloys was electrolytic iron. The analyzed compositions of the seven alloys are given in Table 3. The alloys were first cast into ingots. Each ingot was soaked at 1260°C and subsequently

rolled to 16.5-mm thick plate in five passes. The plates were then austenitized for 30 min at a temperature between 915°C and 926°C, then air cooled to room temperature.

The model iron alloys were irradiated in various geometrical forms. The alloys, for which microstructural characterizations are reported here, were irradiated in the form of C_v specimens and 8-mm diameter x 0.5-mm thick wafers. These alloys will be referred to as bulk-irradiated and wafer-irradiated samples, respectively, throughout this report. The model iron alloys were irradiated at ~ 288°C to a neutron fluence of ~ 4.63×10^{19} n/cm^2 (E > 1 MeV).

Table 3 Chemical Compositions of Model Iron Alloys[a]

Designation	Composition (Wt-%)						
	C	Mn	P	Ni	Cu	N	O
Reference Iron	0.013	0.018	0.003	0.018	<0.005	0.004	0.11
Fe-0.3Cu	0.013	0.013	0.004	0.012	0.28	0.004	0.12
Fe-0.3Cu-0.4Ni	0.010	0.017	0.003	0.37	0.27	0.005	—[b]
Fe-0.3Cu-0.7Ni	0.014	0.017	0.005	0.73	0.25	0.006	0.12
Fe-0.7Ni	0.010	0.017	0.003	0.74	<0.005	0.004	——
Fe-0.7Ni-0.025P	0.010	0.015	0.023	0.69	0.009	0.005	0.11
Fe-0.7Ni-0.025P-0.3Cu	0.012	0.013	0.023	0.70	0.25	0.004	0.13

[a] Hot rolled to 16.5-mm gage
Heat treatment: 915°C, 1/2 h, air cool
Irradiation condition: Temperature: ~ 288°C
Average fluence: ~ 4.63×10^{19} n/cm^2, E > 1 MeV
Specimen: (a) Charpy-V notch
(b) TEM discs
(c) Wafers
(d) Rolled wedges
(e) Tensile specimens

[b] Not analyzed

2.2 Experimental Procedures

2.2.1 Experimental Procedures for Scanning Electron Microscopy

The fracture surfaces of irradiated and unirradiated steel C_v specimens were prepared for SEM examination. Normal degreasing and

ultrasonic cleaning techniques were found to be inadequate. Repeated applications of a cellulose acetate replica were required to obtain reasonably clean specimens. Special lead holders were designed and built to facilitate transportation and handling of the cut specimens in the electron microscope.

All specimens were examined in a JEOL 35 CM scanning electron microscope. The ductile and brittle fracture morphologies and the presence of any unusual fractographic features were noted and photographed. Quantitative measurements of void size were performed on a few specimens under a set of standard operating conditions to ensure internally consistent results.

2.2.2 Experimental Procedures for Transmission Electron Microscopy

Thin foils for TEM analysis were prepared by chemical thinning of 0.5-mm thick wafers to a thickness of ~ 0.08 mm in a solution of 85 parts H_2O_2, 10 parts H_2O, and 5 parts HF acid. Then, 3-mm discs were punched out of the thinned wafers and jet-polished until an electron transparent region was obtained. The best results were obtained with an electrolyte of 750-mL methanol, 450-mL n-butyl alcohol, and 45-mL perchloric acid at -60°C with an applied potential of 20-30 volts and a current of 5-20 mA.

Single-stage carbon extraction replicas were made of polished and etched surfaces and of fracture surfaces of selected steel specimens to aid the analysis of their carbide microstructures. Identification of specific carbides was made on the basis of selected area diffraction patterns, energy-dispersive X-ray microanalysis and particle size and morphology.

The specimens were examined in a JEOL-200CX scanning transmission electron microscope with an accelerating potential of 200 kV. This microscope is located in the Department of Materials Science and Engineering, University of Florida, and is equipped with an energy-dispersive X-ray detection (EDS) and an electron loss spectrometer (EELS) for elemental analysis. Typical investigations involved the use of conventional bright field (BF), centered dark field (CDF), and selected area diffraction (SAD) to analyze the carbide and defect microstructures. Contrast experiments on the defect structures were performed under two-beam dynamical conditions. The weak-beam microscopy technique was employed for imaging very small defects. Additional replicas were examined in a Phillips 400 FEG electron microscope located at the Oak Ridge National Laboratory (ORNL).

2.2.3 Experimental Procedures for Field Ion Microscopy/Atom Probe

Specimens were prepared for FIM/AP/IAP analysis by first cutting 0.4-mm square by 1-cm long blanks from the appropriate bulk material form. For the irradiated alloys, the blanks were cut from the C_v specimens. The blanks were then suspended vertically in a chemical polishing solution of 85 parts H_2O_2, 10 parts H_2O, and 5 parts HF acid

to produce a rough circular taper along the length of the blank. A sharp tip was formed by electropolishing the specimen as it was manipulated through a droplet of electrolyte suspended on a platinum ring. The electrolyte contained 600-mL methanol, 450-mL n-butyl alcohol, and 22.5-mL perchloric acid and was cooled to a temperature below -60°C. An applied potential between 12-20 volts produced the best polishing conditions.

The preliminary examination of the specimen tips was performed using the field ion microscope/imaging atom probe (FIM/IAP) at the University of Florida. Then, the specimens were transported to the Oak Ridge National Laboratory where they were examined in the field ion microscope/atom probe (FIM/AP).

2.2.4 Experimental Procedures for Auger Electron Spectroscopy

To study the phosphorus segregation to particle/matrix interfaces, scanning Auger microscopy (SAM) was conducted on specimens of an irradiated and an unirradiated steel alloy containing phosphorus (Code 67C). Specimens were broken in-situ and analyzed in a PHI 660 system. The small-beam capability (~ 100 Å) with high-beam current makes it possible to perform SEM-type studies in combination with AES analysis on small surface features.

3. MICROSTRUCTURAL CHARACTERIZATION

3.1 Unirradiated Materials

3.1.1 Iron Alloys

The microstructures of unirradiated iron alloys have been discussed in detail in Reference 22. The most significant aspects are summarized here.

The TEM analysis of thin foils revealed the formation of disc-shaped precipitates, which lie parallel to $\{100\}_\alpha$ planes, on dislocations and in the matrix. The extent of in-matrix precipitation was significantly increased in the copper-containing alloys as shown in Fig. 2. Nickel modified this effect of copper and the alloy Fe-0.3Cu-0.7Ni showed a fewer number of in-matrix precipitates. Phosphorus seemed to have an effect similar to that of nickel, i.e., to further retard the in-matrix precipitation when added to a high Cu-high Ni alloy.

The in-matrix precipitates were distributed inhomogeneously, particularly in the nickel-containing alloys. During ingot solidification, Ni is pushed in between dendrite arms. Since nickel is a very slow diffuser in iron, the heat treatments given to these iron alloys did not homogenize the composition. During cooling from the austenite phase, the high nickel regions transform to ferrite last and, consequently, the concentration of copper, which is more soluble in austenite, will be higher in these regions. This inhomogeneity in copper composition results in an inhomogeneous distribution of precipitates.

Within the resolution of TEM, no apparent nucleation sites could be determined for the precipitates formed in the matrix. These precipitates showed a flower-like image contrast. It was found that more than one precipitate had formed from a common origin. The $g \cdot R = 0$ criterion for invisibility, where g is a unit vector perpendicular to the diffracting planes and R is the displacement vector perpendicular to the precipitate plate, was used for distinguishing between α''-nitrides and ε-carbides (Ref. 26). As demonstrated in Fig. 3, almost no precipitates appeared or disappeared upon tilting from the $g = 200$ reflection to the $g = 020$ reflection. As will be shown in later sections, α''-nitride does disappear under the $g \cdot R = 0$ condition. The image contrast (Ref. 27), the absence of visibility/invisibility criterion (Ref. 26), and the higher carbon content suggest that the precipitates consist mainly of ε-carbides.

A recent quench-aging study of the iron alloys has confirmed the effect of copper on enhancing the in-matrix nucleation of ε-carbides (Ref. 28). It has been suggested (Ref. 28) that copper-vacancy pairs formed in a α-iron at high temperatures act as sites for the nucleation of ε-carbide at low temperatures.

Fig. 2 TEM micrographs showing the precipitate microstructures of unirradiated (a) reference iron and (b) Fe-0.3Cu alloys. $[111]_{\alpha}$ zone.

BEST COPY AVAILABLE

Fig. 3 TEM micrographs showing the ε-carbide platelets using (a) g = 200 and (b) g = 020 reflections. $[001]_{\alpha}$ zone.

BEST COPY AVAILABLE

3.1.2 Steel Alloys

The microstructures of the steel alloys were characterized by TEM analysis of thin foils and extraction replicas. The latter specimens were used for chemical analysis of carbides. The detail of microstructural analysis of unirradiated steel alloys can be found in References 21 and 23. The identification of specific carbides was accomplished by analyzing selected area diffraction patterns and energy-dispersive X-ray spectra. The carbide microstructures of all the steel alloys examined were the same and consisted of an inhomogeneous distribution of M_3C and M_2C carbides in a bainitic microstructure. We did not encounter any M_6C carbides, but this does not eliminate the fact that some M_6C carbides may have existed at boundaries.

The carbides were categorized based on their (a) size [large, > 1 μm; medium, 1-0.2 μm; small, 0.2-0.5 μm; fine, < 0.05 μm], (b) shape [spherical, elongated, irregular, needle], and (c) location [grain boundary, inter-lath, intra-lath]. There were indications of lamellar cementite plates, which suggest that the austenitizing treatment of 1 h at 900°C (Ref. 25) was not long enough to dissolve all the carbides.

Figure 4 shows TEM micrographs of thin foil and extraction replica specimens of the high P-low Cu (Code 67C) steel. These micrographs are representative of all the steel alloys examined. A high dislocation density, typical of tempered martensite/bainite microstructures, was found in thin foils, as shown in Fig. 4a. The inhomogeneity of the carbide distribution is represented in Fig. 4b.

3.2 Irradiated Materials

3.2.1 Iron Alloys

The microstructures of irradiated iron alloys were characterized using TEM and FIM/AP techniques. The FIM/AP study was conducted at the Metals and Ceramics Division of ORNL under the supervision of Dr. M. Miller (Ref. 29). This section is divided into three parts: (1) Defect Structure, where the results of TEM analysis of dislocation loops are reported; (2) Carbide and Nitride Structures, which separate from the defect structure deserves an independent discussion; and (3) Ultra-Fine Structure, where the results of FIM/AP analysis are discussed. The reader is referred to References 23 and 24 for a comprehensive report of the microstructural analysis of the irradiated iron alloys.

3.2.1.1 Defect Structure

Neutron irradiation had introduced observable defects in all irradiated alloys examined. These defects were distributed homogeneously in the matrix, in contrast to the reported inhomogeneous distribution (or clustering) of defects in neutron irradiated iron alloys irradiated to higher fluences ($> 10^{20}$ n/cm^2) than this study, but at comparable

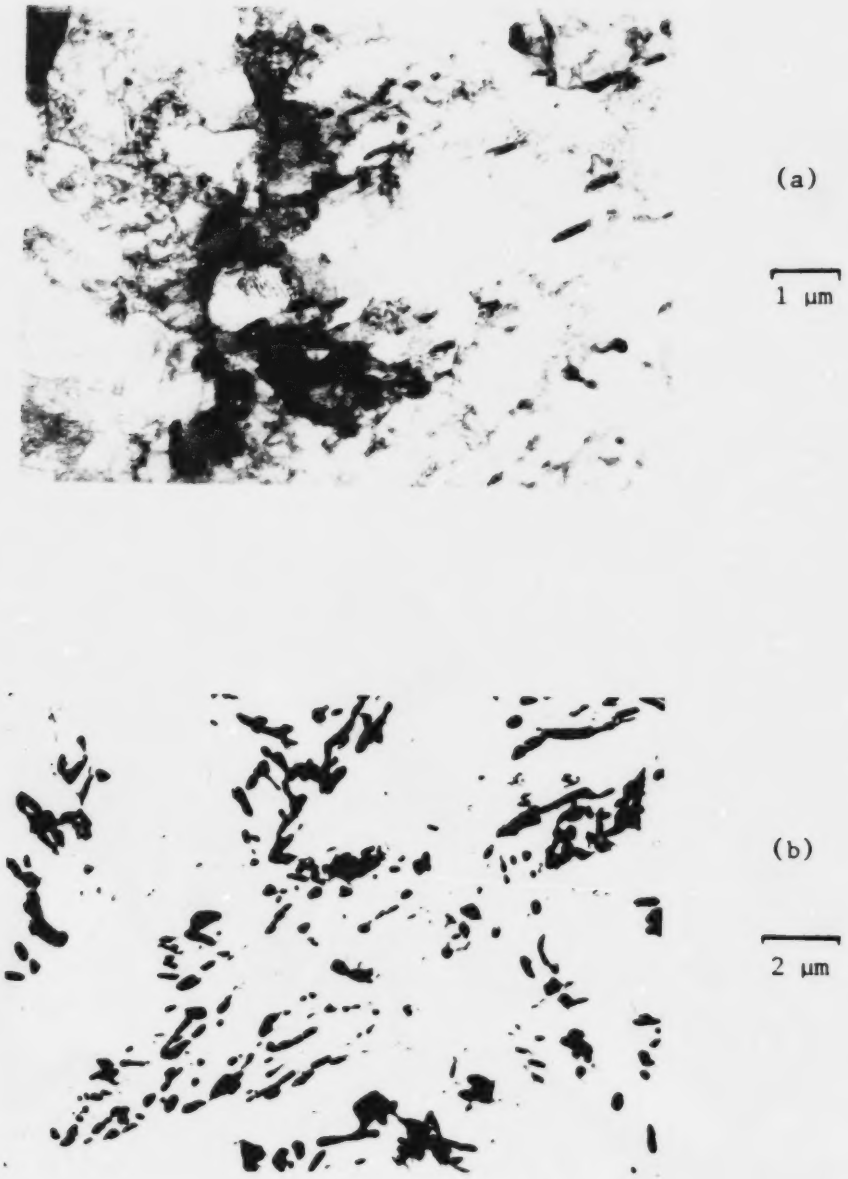

Fig. 4 TEM micrographs showing the general microstructure of the steel alloys before irradiation. (a) Thin foil and (b) single-stage carbon extraction replica from a polished and etched surface.

BEST COPY AVAILABLE

irradiation temperatures (Refs. 9 and 30). Tilting experiments on those defects that were large enough for analysis showed they are near-edge dislocation loops of interstitial nature. Both a<100> and a/2<111> Burgers vectors were identified. The size and number density of observable loops and the fraction of dislocation loops with a<100> and a/2<111> Burger vectors were found to depend on the composition of the iron alloys, as shown in Table 4.

Table 4 Results of Quantitative Analysis of Observable Dislocation Loops in Irradiated Iron Alloys

Alloy	$\overline{d}$[a] (A)	N[b] (cm^{-3})	f<100>[c] (%)
Reference Iron	86	3.7×10^{15}	91
Fe-0.3Cu	32	4.8×10^{15}	75
Fe-0.3Cu-0.4Ni	~22	$\sim 1.0 \times 10^{16}$	d
Fe-0.3Cu-0.7Ni	~12	$\sim 1.0 \times 10^{16}$	d
Fe-0.7Ni	28	6.5×10^{15}	25
Fe-0.7Ni-0.025P	d	d	d
Fe-0.7Ni-0.025P-0.3Cu	d	d	d

a $\overline{d}$ = mean defect diameter
b N = number density of defects
c f<100> = fraction of dislocation loops with a<100> Burgers vector
d too small to be analyzed by TEM

Figures 5 through 11 present the defect microstructure of the iron alloys examined, accompanied by the size distribution of dislocation loops. Weak-beam technique was employed to reveal the fine defects; however, the number density reported for very fine loops should be regarded as an approximate value and most probably an underestimation of the real value. The number density reported in Table 4 includes those defects with black spot contrast. These defects are most probably very fine dislocation loops rather than copper or phosphorus clusters. The former clusters have been reported to show no visible contrast and the latter clusters, as will be shown later, are too small to be imaged in TEM. The defects in Fe-0.7Ni-0.025P and Fe-0.7Ni-0.025P-0.3Cu alloys were too small for the size distribution analysis.

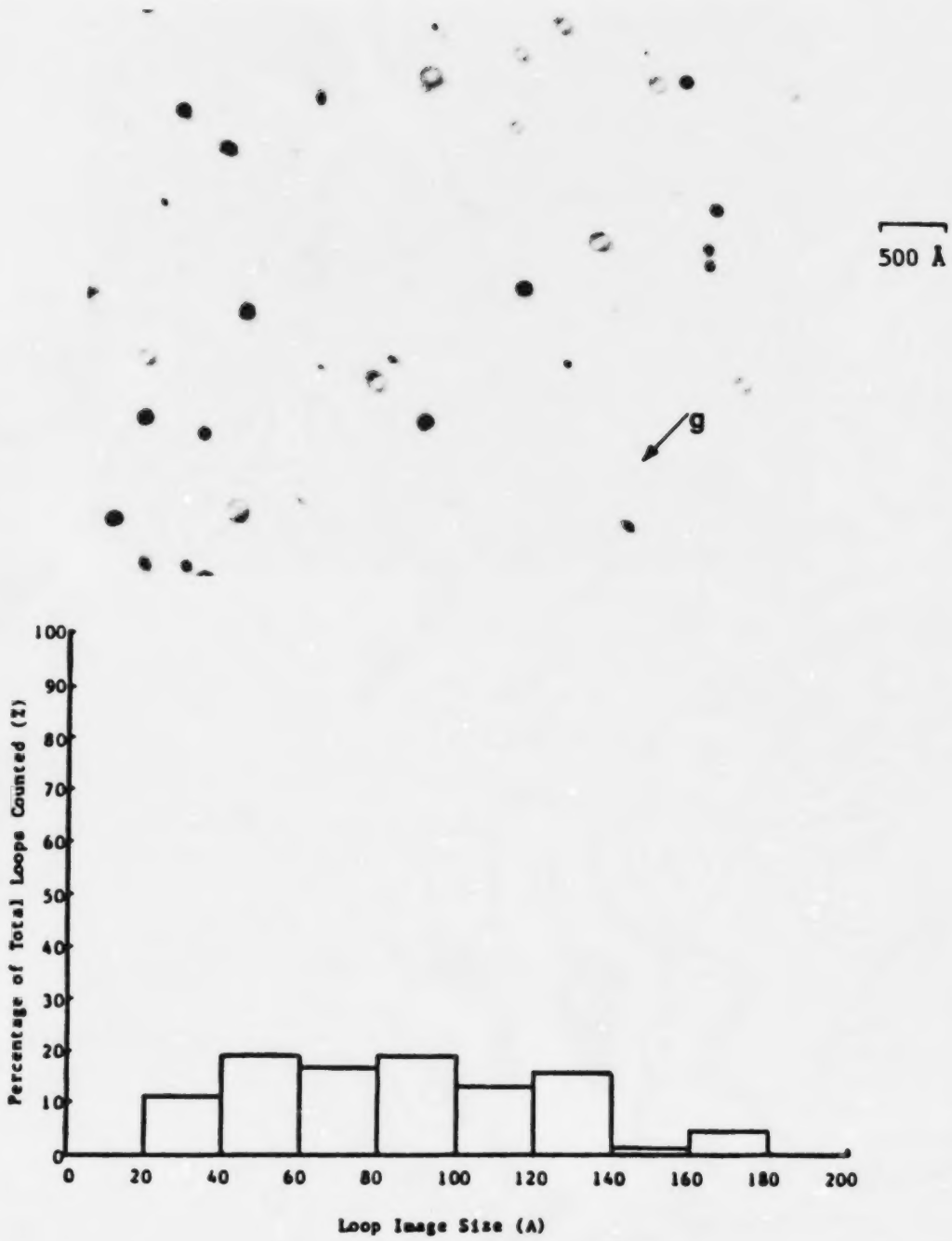

Fig. 5 TEM micrograph showing the defect structure in the irradiated reference iron alloy accompanied by the defect size distribution. Near $[011]_{\alpha}$ zone axis; g = 011.

BEST COPY AVAILABLE

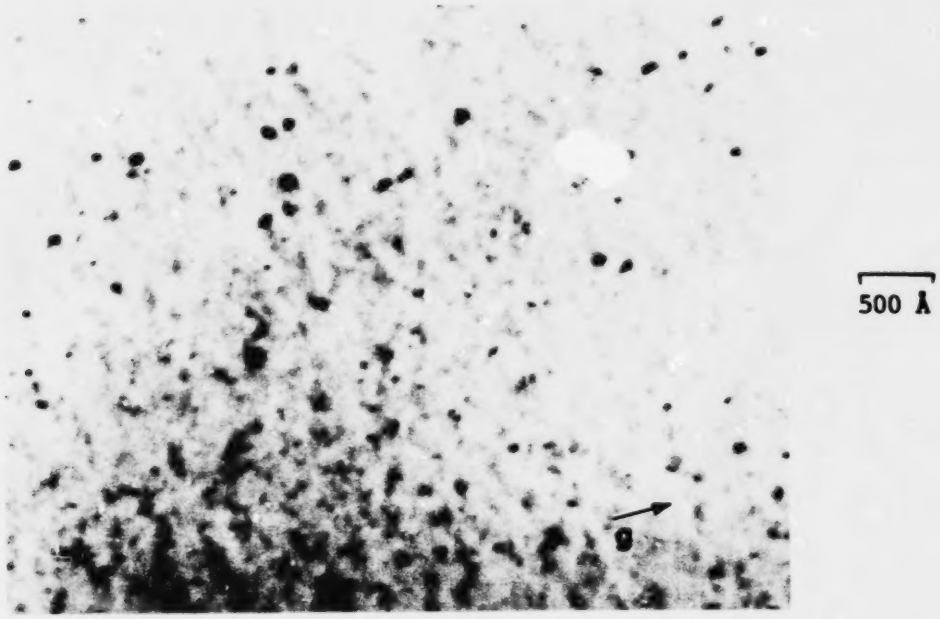

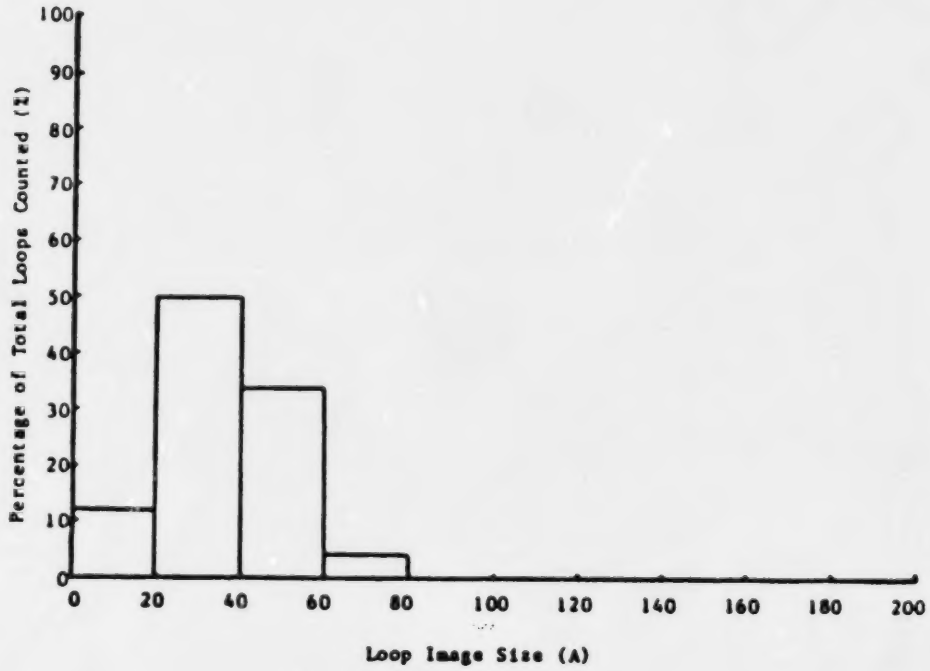

Fig. 6 TEM micrograph showing the defect structure in the irradiated Fe-0.3Cu iron alloy accompanied by the defect size distribution. Near $[011]_{\alpha}$ zone axis; g = $01\bar{1}$.

BEST COPY AVAILABLE

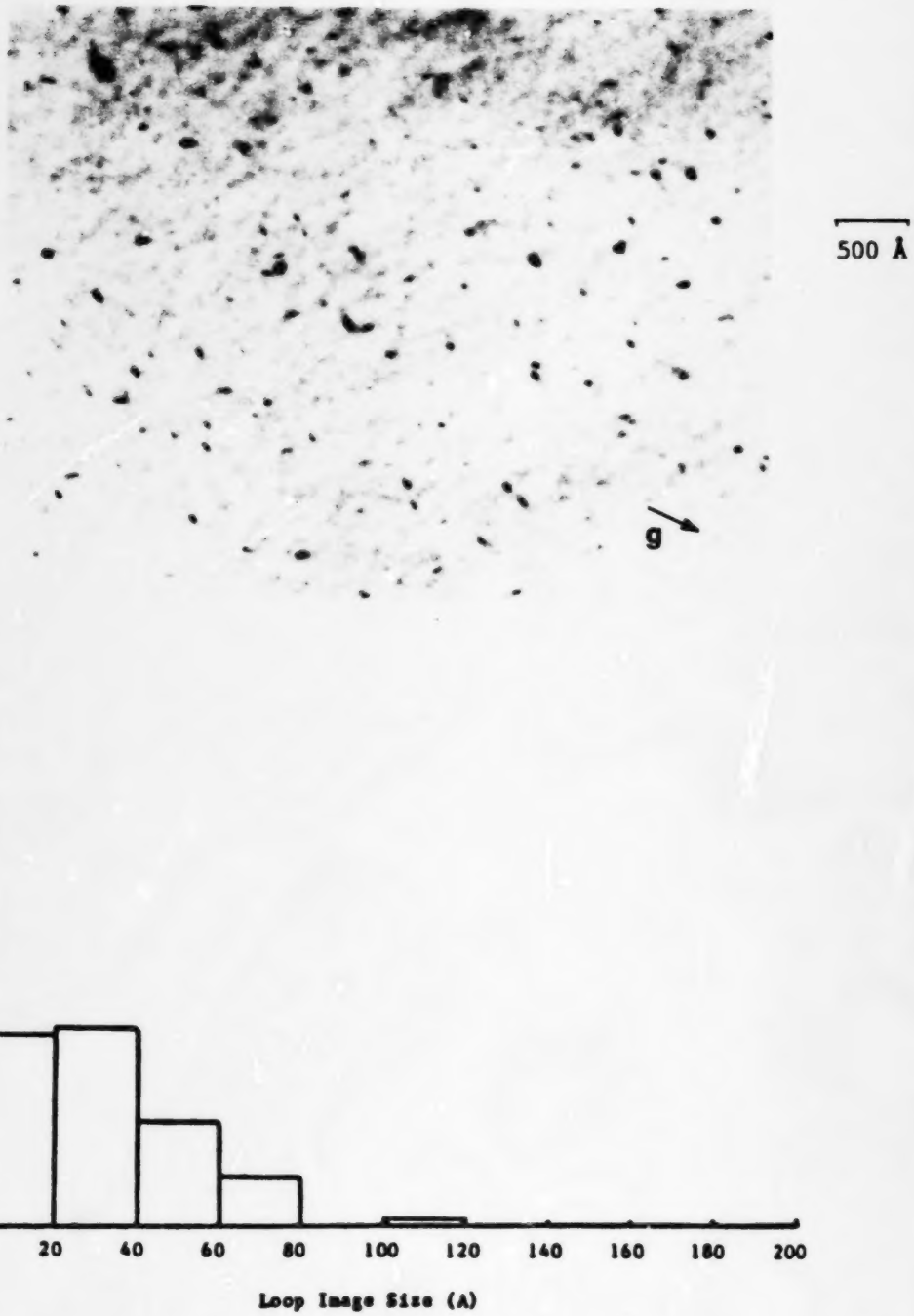

Fig. 7 TEM micrograph showing the defect structure in the irradiated Fe-0.7Ni iron alloy accompanied by the defect size distribution. Near $[011]_{\alpha}$ zone axis; $g = 01\bar{1}$.

BEST COPY AVAILABLE

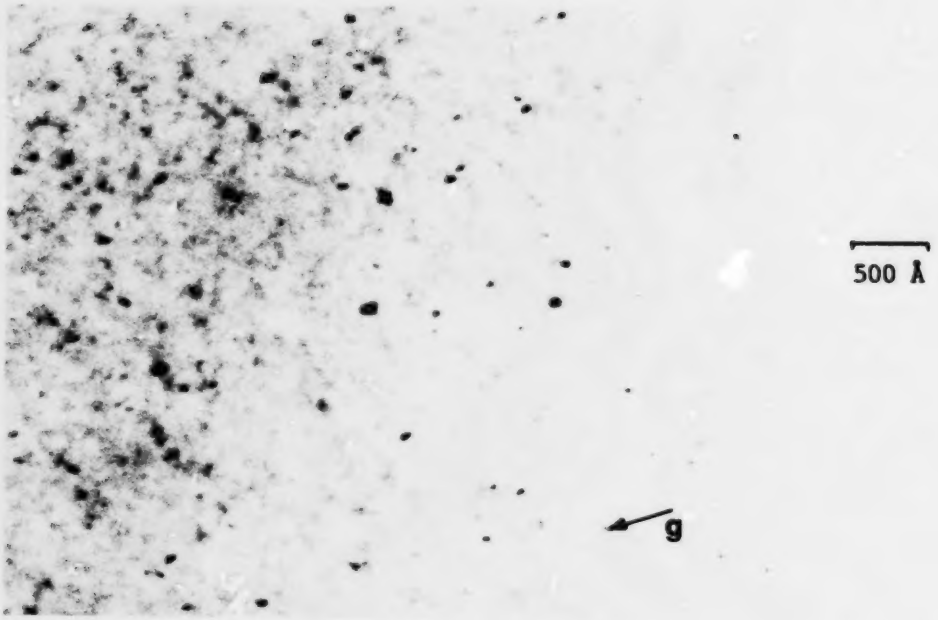

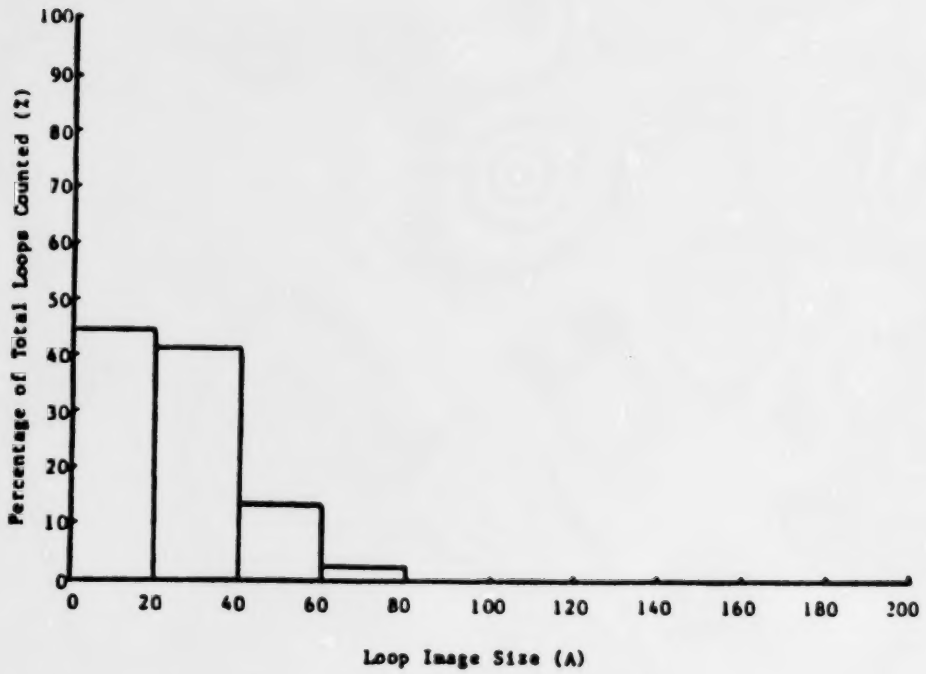

Fig. 8 TEM micrograph showing the defect structure in the irradiated Fe-0.4Ni-0.3Cu iron alloy accompanied by the defect size distribution. Near $[011]_{\alpha}$ zone axis; $g = 01\bar{1}$.

BEST COPY AVAILABLE

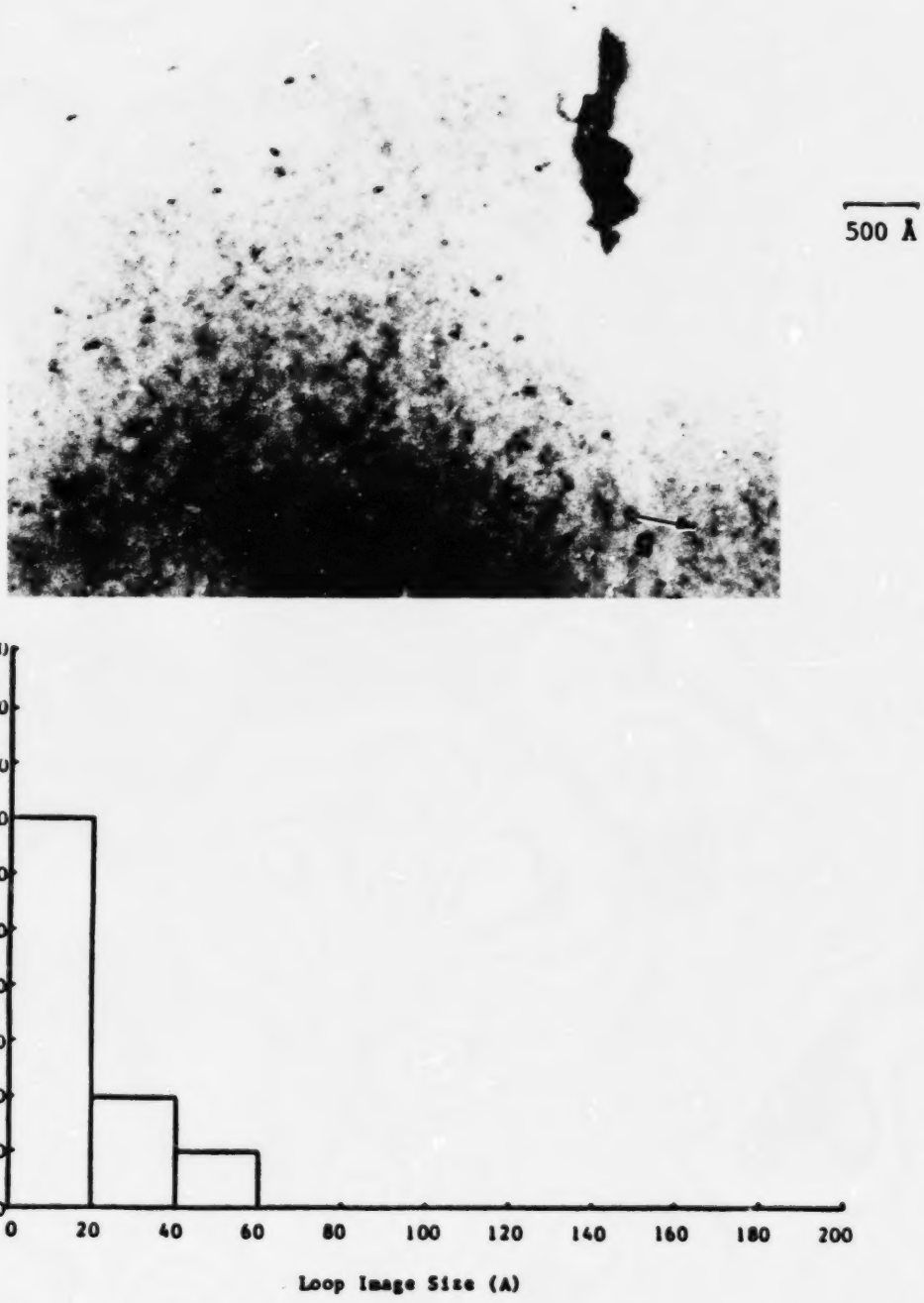

Fig. 9 TEM micrograph showing the defect structure in the irradiated Fe-0.7Ni-0.3Cu iron alloy accompanied by the defect size distribution. Near $[011]_{\alpha}$ zone axis; $g = 01\bar{1}$.

BEST COPY AVAILABLE

Fig. 10 TEM micrograph showing the defect structure in the irradiated Fe-0.7Ni-0.025P iron alloy. Near $[011]_{\alpha}$ zone axis; g = $01\bar{1}$.

BEST COPY AVAILABLE

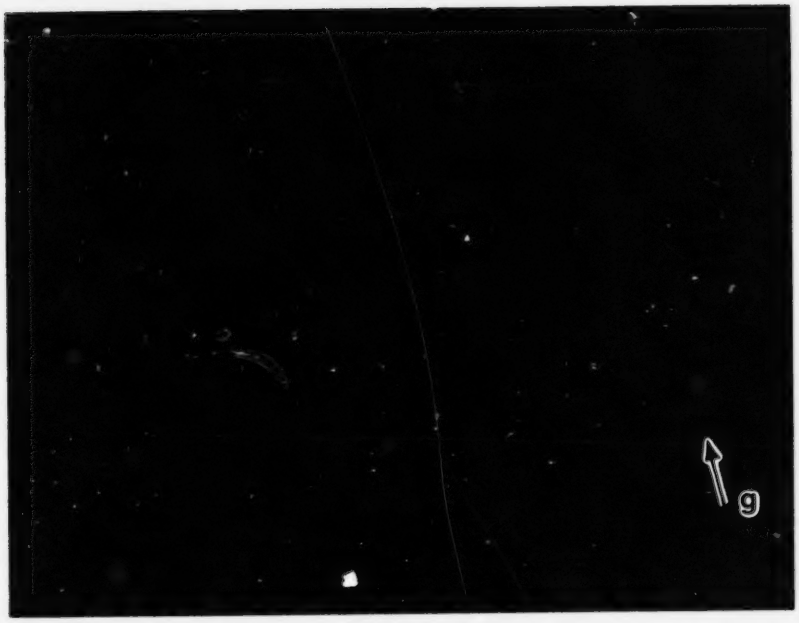

500 Å

Fig. 11 TEM micrograph showing the defect structure in the irradiated Fe-0.7Ni-0.025P-0.3Cu alloy under weak-beam conditions. Near $[011]_{\alpha}$ zone axis; $g = 01\bar{1}$.

BEST COPY AVAILABLE

The above results show that additions of Cu, Ni, and/or P decrease the size of irradiation-induced defects significantly and perhaps increase the number density of the defects. Phosphorus is the most potent element in reducing the size of defects. The predominant type of Burgers vector of the loops observed in the reference iron alloy was found to be a<100> type. The presence of copper (Fe-0.3Cu) in iron increased the fraction of a/2<111>-type dislocation loops. The presence of nickel (Fe-0.7Ni) had a dramatic effect upon the Burgers vector of the loops. The percent of a/2<111> loops increased from 9% in the reference iron to 75% in the Fe-0.7Ni alloy. Due to the small size of defects, the combined effect of copper and nickel, and the effect of phosphorus on the type of Burgers vector could not be evaluated. The coexistence of a/2<111> and a<100> dislocation loops has been reported by Gelles in Fe-Cr ferritic steels (Ref. 31). He found that a<100> Burgers vector were predominant in the Fe-3Cr alloy but changed to predominantly a/2<111> Burgers vector at higher chromium concentrations. The dependency of the Burgers vector of dislocation loops upon impurity has also been reported by Horton (Ref. 30).

As far as the effects of copper and phosphorus on defect size are concerned, our results are qualitatively in agreement with Smidt and Sprague results (Ref. 9), i.e., additions of these elements reduce the mean diameter and increase the number density of dislocation loops. Wagner et al. (Ref. 13) have also reported a similar effect of copper on defect size distribution. Contrary to Smidt and Sprague results (Ref. 9), we found a significant effect of nickel on the defect structure generated by neutron irradiation. It should be noted that their samples were irradiated to a higher fluence ($4.5 \times 10^{20} n/cm^2$) than the fluence used in this study.

Within the resolution of TEM (~ 20 Å), no voids were observed in the irradiated iron alloys. Recent results of SANS experiments performed on the same alloys examined in this study (Ref. 32) show the existence of defects of the order of 12-15 Å in diameter in the reference and Fe-0.7Ni alloys. These defects have been suggested to be voids. However, the FIM/AP study of these alloys (Ref. 29) showed no void formation.

The behavior of dislocation loops near dislocation lines, low-angle boundaries and grain boundaries was another area of investigation. Zones denuded of dislocation loops were observed in the reference iron alloy near many low-angle boundaries and dislocation lines as shown in Fig. 12. However, this behavior was not observed in any of the alloys containing nickel, copper, and/or phosphorus. In fact, alloys containing copper or phosphorus showed formation of a high density of very large dislocation loops adjacent to dislocation lines. These large loops were preferentially distributed along one side of the dislocation line. Similar damage structure has been reported for neutron irradiation molybdenum (Ref. 16) and high purity iron (Ref. 33). Figure 13 shows the formation of large dislocation loops in the vicinity of dislocations in Fe-0.7Ni-0.025P and Fe-0.3Cu alloys. The addition of nickel (Fe-0.7Ni) did not cause formation of large dislocation loops and, in fact, it reduced the extent of this phenomenon in the copper-containing alloys.

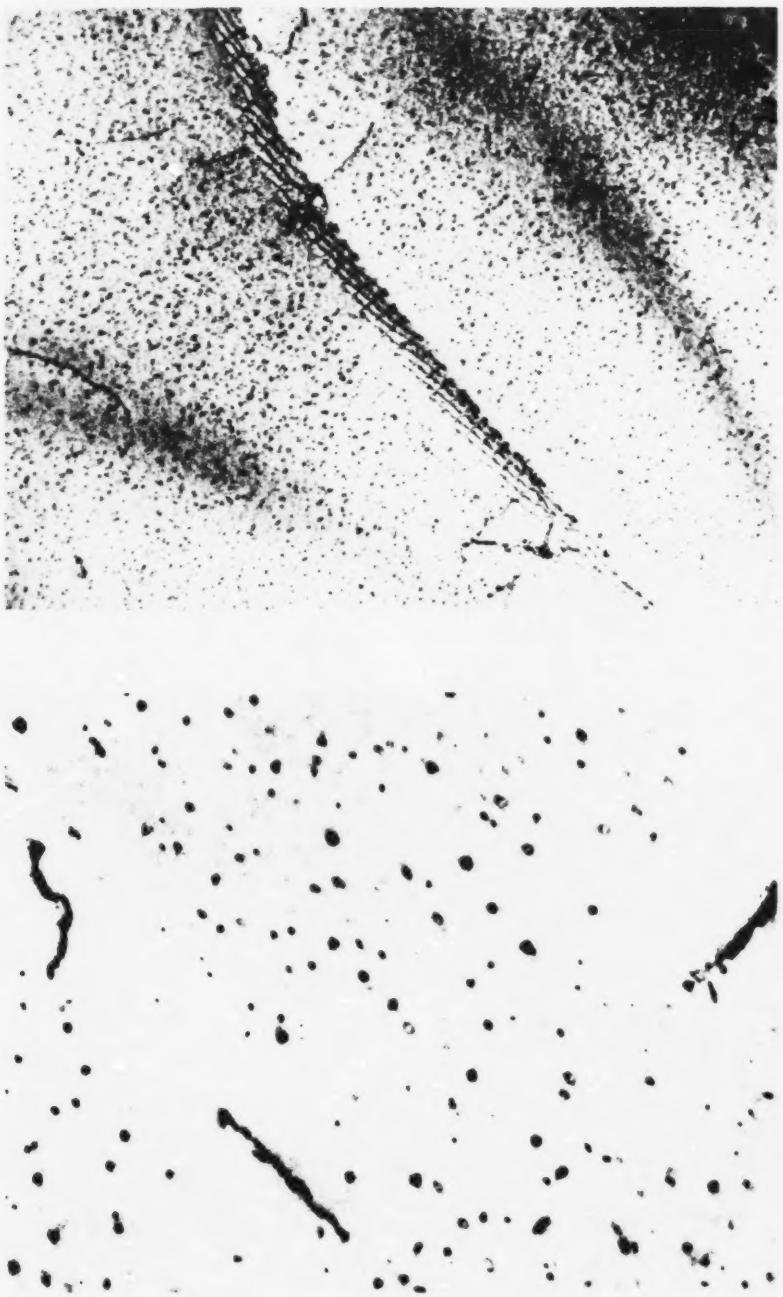

Fig. 12 TEM micrographs showing denuded zones of defects in the irradiated reference iron alloy around (a) a low-angle boundary and (b) dislocations. Near $[011]_{\alpha}$ zone axis.

BEST COPY AVAILABLE

Fig. 13 TEM micrographs showing the formation of large dislocation loops adjacent to dislocations in (a) Fe-0.7Ni-0.025P and (b) Fe-0.3Cu.

BEST COPY AVAILABLE

To discuss the possible mechanisms responsible for the above observations, first we have to consider the nucleation and growth of interstitial dislocation loops. Eyre and Bullough (Ref. 34) have suggested that, in BCC metals, interstitial loops form by the collapse of a disc of point defects in a (110) plane. Such a faulted loop with a Burgers vector of a/2<110> can unfault by two possible shear mechanisms:

$$a/2\langle 110\rangle + a/2\langle 001\rangle = a/2\langle 111\rangle \qquad (1)$$

$$a/2\langle 110\rangle + a/2\langle 1\bar{1}0\rangle = a\langle 100\rangle \qquad (2)$$

Reaction (1) is energetically favored at all irradiation temperatures. Little, Bullough, and Wood (Ref. 35) calculated the relative probability of a<100> and a/2<111> loop formation. Their calculations showed a very small, but finite, probability for a<100> loop formation. The observation of predominantly a<100> loop in an Fe-Cr ferritic steel has been attributed to the stronger bias of a<100>-type dislocations, which have a large Burgers vector, for interstitial atoms. Initially, loops with a b = a/2<111> are the predominant loop type nucleated. Each a<100> loop is surrounded by the relatively neutral a/2<111>-type loops. The latter loops act as sinks and absorb the net vacancy flux created by the preferential interstitial capture of the isolated a<100> loops. Eventually, the a/2<111> interstitial loops disappear and a<100> loops grow. Following this model in ferritic steels, any alloying/impurity element that reduces the number of interstitial defects available for the growth of a<100> loops will increase the number density of dislocation loops by increasing the number of a<111> loops that survive. Consequently, both the size and the total area of dislocation loops will be reduced.

The most important effect of solute atoms on the evolution of defect structure during irradiation is the trapping of point defects. Vacancies have been suggested to be associated with copper in α-iron (Refs. 9, 36, and 37). The association of copper with vacancies have been suggested to affect the evolution of the defect structure directly by providing nucleation sites for defect aggregates and/or indirectly by influencing the kinetics of the defect motion (Ref. 9). Smidt and Sprague (Ref. 9) have argued that vacancy trapping reduces the interstitial concentration, and therefore it would decrease the homogeneous nucleation rate of interstitial defects. Therefore, they have suggested a heterogeneous nucleation mechanism in which copper-vacancy pairs act as nucleation sites. However, a simple copper-vacancy pair is expected to act as a recombination site rather than a nucleation site. In fact, Little (Ref. 38) has concluded that as a result of recombination, growth of both voids and dislocation loops is reduced due to the reduced number of available point defects. Obviously, the effect of vacancy trapping on the evolution of defect structure should be sought in the growth process rather than in the nucleation of the loops. As shown in Figs. 5 through 9, the reference iron alloy has a broad size

distribution of defect aggregates, while the other alloys show a much narrower defect size distribution. This difference in size distribution clearly indicates a significant change in the growth rate and/or survival rate of the dislocation loops. It should be noted that the number density of defects observed after irradiation does not represent the true number of nucleation sites since dislocation loops themselves act as sinks and may shrink and disappear.

Based on the above discussion, we present the following model to account for the reduction in size and the increase in number density of dislocation loops due to the addition of copper. The interstitial loops nucleate as a<100> loops (Ref. 34), which mostly unfault to a/2<111> loops with a small fraction of a<100> loops (Ref. 35). The vacancy trapping by copper reduces the interstitial concentration, and consequently the a<100> loop growth rate is decreased. Following Little et al. (Ref. 35), as a result of the lower growth rate of a<100> loops, the a/2<111> loops see a smaller net vacancy flux, which is created by preferential interstitial capture of the a<100> loops, and their shrinkage rate will be reduced. This proposed mechanism accounts for both the smaller size of the defect aggregates and the larger fraction of a/2<111> loops in the alloys containing Cu.

Our results indicate that nickel is a more influential element than Cu in modifying the size distribution of dislocation loops. Large concentrations of Ni is known to increase the pre-exponential term of the vacancy diffusion coefficient in austenitic steels; however, the mechanism of this effect is not known (Ref. 39). If nickel increased the diffusivity of vacancies in BCC crystals, then we would expect an opposite effect of Ni on microstructure, i.e., larger interstitial dislocation loops with a lower number of a/2<111> loops. Also, nickel would be expected to decrease the swelling rate in ferritic steels, similar to austenitic steels. The results reported by Smidt and Sprague (Ref. 9) indicate that, in fact, nickel increases both the number density and the size of voids in ferritic iron alloys. This result is consistent with our observation of small dislocation loops with a high density of a/2<111> loops in the Fe-0.7Ni alloy. The interaction of Ni with point defects in BCC iron has not been explored. Nickel has an atomic radius very close to iron; therefore, from the atomic size point of view, it does not have a tendency to bind with point defects. The effect of nickel on the electronic and magnetic states of iron atoms (Ref. 40) may account for any interaction between nickel and point defects in BCC iron crystals.

Similar to copper and nickel, phosphorus also reduces the size of dislocation loops. Although due to the small size of defect aggregates we could not identify their Burgers vector, we expect that phosphorus also retards the growth of a<100> loops. Positron annihilation results (Ref. 41) indicate a strong binding between phosphorus and vacancies in an austenitic steel. It is possible that this interaction also exists in ferritic alloys.

Interstitial impurities, i.e., carbon, nitrogen, and oxygen, are known to trap vacancies; however, the stability of such complexes at 288°C is questionable. The iron alloys studied in this investigation had

similar interstitial contents, and we were not concerned with the effect of these elements. However, the effect of substitutional solutes, M, can be modified by interstitial elements, I, through the formation of M-V-I complexes. On the basis of enhanced in-matrix precipitation of ε-carbides by copper, we suspect that formation of Cu-V-C complexes are probable.

The addition of copper and phosphorus was observed to cause the formation of many large dislocation loops adjacent to network dislocations. Robertson (Ref. 33) has observed that the extent of formation of large dislocation loops in the vicinity of low-angle boundaries in high purity irons irradiated at ~ 80°C depends on the interstitial impurity content. Therefore, he has suggested that interstitial carbon and nitrogen atoms form atmospheres around the dislocation and trap the in-flowing point defects and thereby form stable loop nuclei. This mechanism cannot explain the absence of higher density and larger dislocation loops and the existence of the denuded zones around the low-angle boundaries in the reference iron alloy examined in this investigation. Furthermore, interstitial impurities interact more strongly with vacancies than with interstitial iron atoms. However, the large loops in both this investigation and Robertson's study have been found to be of interstitial nature.

The existence of denuded zones of defect aggregates in the vicinity of sinks in reference iron and the absence of them in iron alloys containing alloying/impurity elements suggest that the strength and the bias of sinks have been altered by the solute atoms due to size and Kirkendall effects. Following Bullough (Ref. 16), the formation of large dislocation loops adjacent to dislocation lines indicates the poisoning of the dislocation lines. The interstitial atoms are attracted to the stress-field of dislocations; however, they are unable to join the core of dislocation lines due to the accumulation of solute atoms. Consequently, a high density of interstitials is generated in the neighborhood of dislocation lines. As a result, the nucleation rate is enhanced and loops grow larger than in the matrix. The nucleation rate of the loops could also be enhanced by the stress-field of the dislocation network.

3.2.1.2 Carbide and Nitride Structures

The microstructural analysis revealed that, as anticipated, ε-carbides had disappeared upon exposure to 288°C due to thermal instability. Cementite particles had formed in the matrix during the early stages of irradiation. Eventually, the grain boundary carbides grew in expense of the dissolution of in-matrix cementite particles. Figure 14a presents a low magnification TEM micrograph showing the typical in-matrix cementite left in irradiated alloys. Figure 14b shows a half-dissolved cementite particle. The number density of cementite particles was very small, and no conclusion could be made on possible effects of alloying/impurity elements on the dissolution of cementite during irradiation.

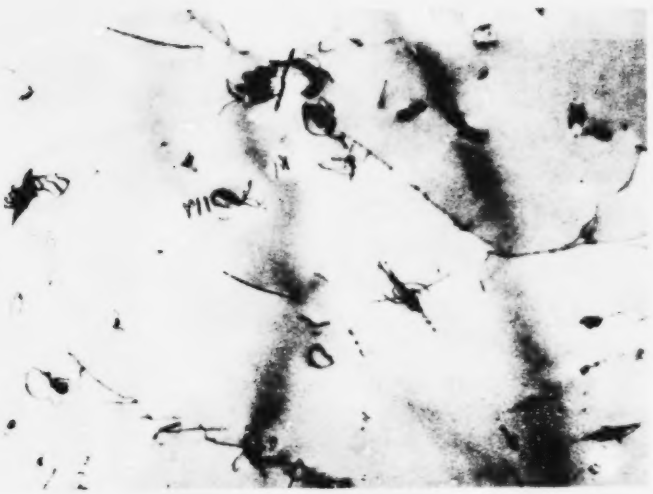

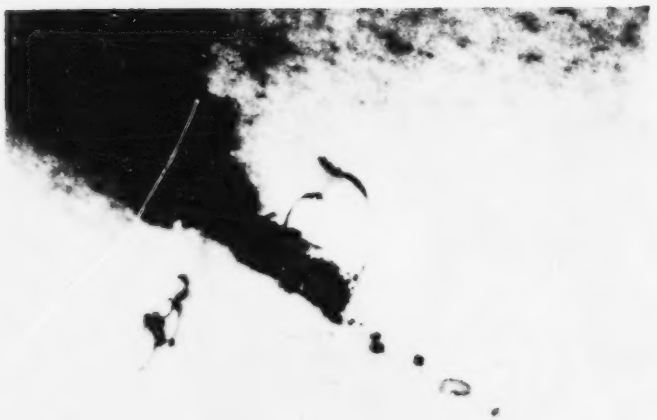

Fig. 14 TEM micrographs showing (a) the typical distribution of in-matrix cementite particles left after irradiation (Fe-0.3Cu-0.4Ni alloy) and (b) a half-dissolved cementite particle in the irradiated Fe-0.7Ni-0.3Cu-0.025P alloy.

BEST COPY AVAILABLE

As was mentioned in the Materials Section, samples were irradiated in wafer and bulk geometries. Although the carbide and defect structures were found to be the same in bulk-irradiated and wafer-irradiated samples, a difference in nitride structure was observed in these samples. Most of the nitrogen content of iron alloys is soluble in the matrix at 288°C (Ref. 42). No nitride precipitates were found in the wafer-irradiated iron alloys. However, TEM foils prepared from the bulk-irradiated samples showed the formation of nitrides on carbides, in-matrix and on dislocations. Figure 15 shows a TEM micrograph showing the formation of precipitates on dislocations and in the matrix. The α"-nitrides were formed as platelets parallel to $\{100\}_\alpha$ planes. Since selected area diffraction patterns could not be obtained from these precipitates due to their very small thickness, the $g \cdot R = 0$ criterion for invisibility (weak or residual contrast), where g is a unit vector perpendicular to the diffracting planes and R is the displacement vector perpendicular to the platelet plane, was used for identifying the α"-nitrides (Ref. 26). Figure 16 demonstrates that near a $[001]_\alpha$ zone axis the precipitates are visible with a $g = 1\bar{1}0$ reflection (Fig. 16a); those with edge-on image parallel to $[100]_\alpha$ direction show weak (or residual contrast) with a $g = 020$ reflection, and those with edge-on image parallel to $[010]_\alpha$ direction disappear (or show residual contrast) with a $g = 200$ reflection. This behavior of the precipitates confirms that they are α"-nitride (Ref. 26). Figure 17 shows the presence of nitrides on a carbide/matrix interface in a bulk-irradiated sample.

The extent of nitride precipitation was found to depend on the alloy content. The reference iron alloy showed a very small number of in-matrix nitrides, and also most of the dislocations were free from precipitates. In fact, in-matrix nitrides could be found easily only in thick regions of thin foils as shown in Fig. 18. It was found that in-matrix nitrides were etched out in the thin areas of foils.

As will be discussed in Section 2.3, the absence of α"-nitride precipitation in the wafer-irradiated samples is due to their faster cooling rate in comparison to the bulk-irradiated specimens. The difference in the extent of nitride precipitation between the reference iron alloy and the other iron alloys can be explained by a consideration of point-defect trapping. It may be speculated that most of the nitrogen atoms are associated with vacancies in the form of stable complexes in the reference iron alloy and therefore are not available for precipitation. However, in the alloys containing Cu, Ni, and/or P vacancies bind with substitutional elements, and therefore nitrogen is free for precipitation upon cooling.

3.2.1.3 Ultra-Fine Structure

The FIM/AP experiments were conducted at ORNL (Ref. 29), and the results are discussed here briefly. Copper clusters and/or precipitates were found in the irradiated copper-containing alloys examined (Fe-0.3Cu, Fe-0.3Cu-0.7Ni, Fe-0.7Ni-0.025P). Almost all of the copper had precipitated, as evidenced by a very low matrix copper content (Ref. 29). The maximum local copper concentration measured for the

Fig. 15 TEM micrograph showing the precipitation of α''-nitrides in the matrix and on a dislocation in the Fe-0.3Cu-0.7Ni-0.025P alloy.

BEST COPY AVAILABLE

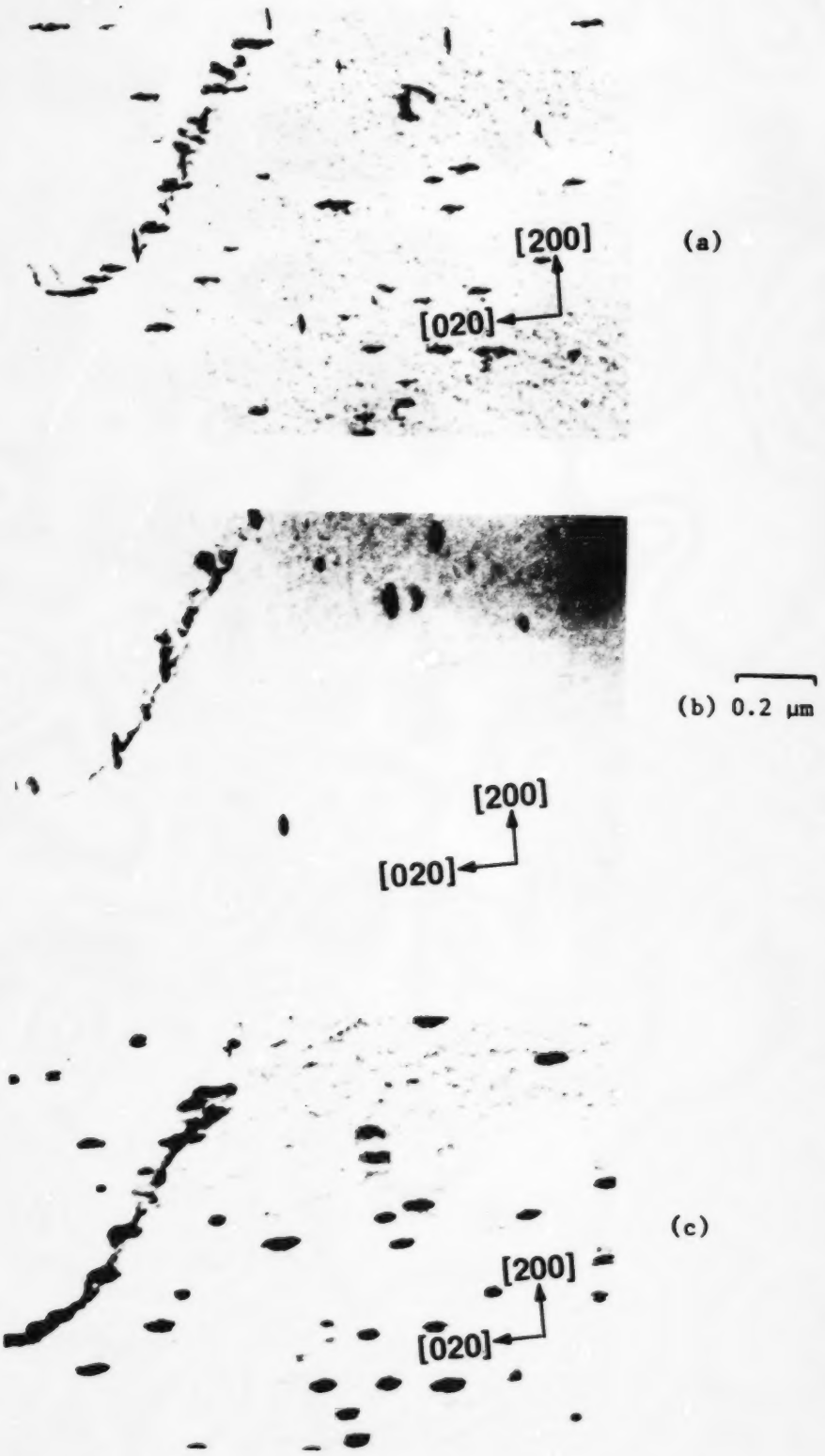

Fig. 16 TEM micrographs showing the precipitates in bulk-irradiated Fe-0.7Ni-0.025P alloy with (a) g = $1\bar{1}0$, (b) g = 020, and (c) g = 200 reflections. Near $[001]_\alpha$ zone axis.

BEST COPY AVAILABLE

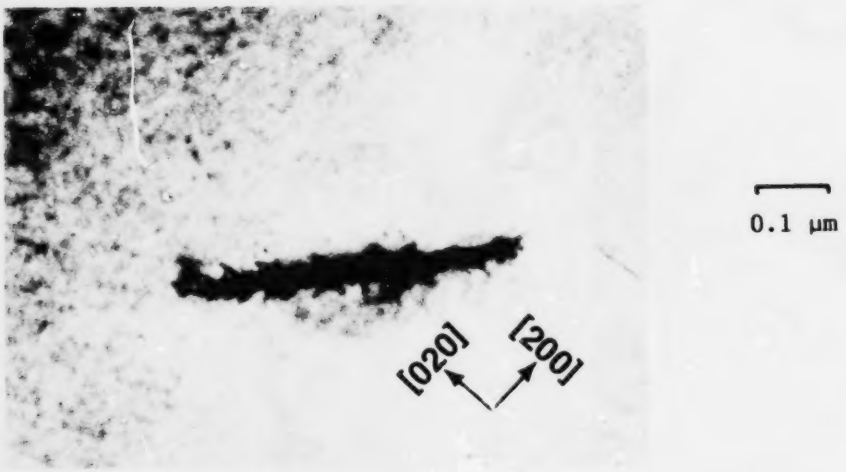

Fig. 17 TEM micrograph showing α''-nitride precipitates on a carbide/matrix interface in a bulk-irradiated Fe-0.7Ni-0.25P alloy. B = [001], g = 110.

BEST COPY AVAILABLE

(a)

0.1 μm

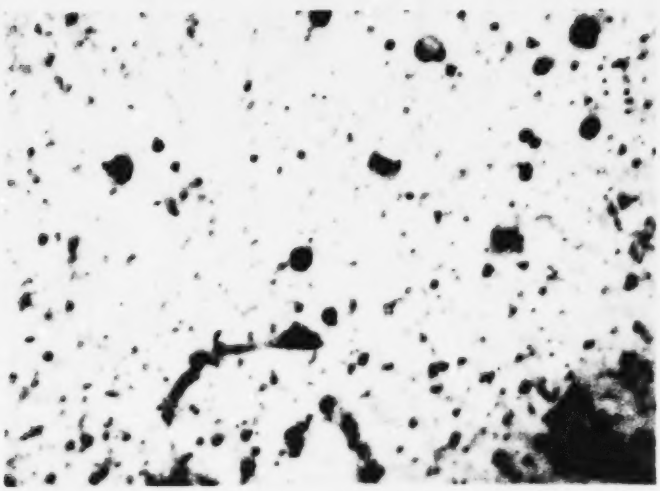

(b)

Fig. 18 TEM micrographs showing the absence of nitride precipitates on dislocations in the bulk-irradiated reference iron reference alloy and demonstrating the foil thickness effect. (a) Thin regions and (b) thick regions.

BEST COPY AVAILABLE

largest precipitate was 58 at. %. This value is consistent with results reported by Goodman et al. (Refs. 43-44), who found a copper content of 51 at. % in a large particle. It should be noted that the local concentration measured depends on the size, geometry, orientation of the particle, and the aperture hole size. Only in the case of particles much larger than the aperture hole, this measured concentration represents the actual particle composition. The precipitation of Cu-rich particles during neutron irradiation of copper-containing iron alloys at ~ 290°C has been reported previously (Refs. 12-14).

The composition profile of a large Cu-containing cluster/precipitate in the Fe-0.3Cu-0.7Ni showed that the nickel content of the particle was enriched by a factor of ~ 7, and a higher enrichment level of ~ 14 over the matrix was measured at the precipitate/matrix interface. Similar enrichment of the Cu precipitate/matrix interface was found in Fe-0.3Cu-0.7Ni-0.025P alloy. Recently, Worall et al. (Ref. 45) have conducted FIM/AP analysis on an age-hardened (unirradiated) iron-copper-nickel alloy. They have reported a nickel-rich shell around the larger overaged FCC copper precipitates with no nickel contained in the precipitate. However, nickel was found to be associated with the smaller underaged coherent BCC copper particles, although it is not possible at these small sizes to determine if nickel has segregated to the interface region. The results of matrix composition (Ref. 29) showed that nickel had remained mainly in the matrix and only a very small fraction of the nickel content is associated with copper clusters/precipitates. This result is consistent with the recent SANS data (Ref. 32) which show that nickel has virtually no effect on the distribution of Cu precipitates formed during irradiation.

In addition to the nickel enrichment, phosphorus enrichment of the copper clusters/precipitates was observed in the Fe-0.3Cu-0.7Ni-0.025P alloy. A total of 25 of the 32 copper clusters/precipitates analyzed contained varying levels of phosphorus. The low phosphorus content of the matrix (Ref. 29) indicate that most of the phosphorus atoms were associated with copper clusters/precipitates. In this alloy, no clusters of phosphorus were found.

Investigation of the irradiated Fe-0.7Ni-0.025P alloy revealed the existence of phosphorus-rich clusters. These clusters were very small in size. Eight phosphorus-rich clusters were detected. Seven of the eight clusters contained less than ~ 20 phosphorus atoms, while the eighth cluster contained ~ 90 phosphorus atoms. Only the larger phosphorus cluster was enriched with nickel. Again, the matrix composition (Ref. 29) indicates that almost all of the phosphorus had clustered during irradiation.

No nickel clustering was detected in any of the irradiated alloys including Fe-0.7Ni alloy. The FIM/AP analysis did not show any indications of void formation in the irradiated iron alloys. The atom probe analysis showed a darkly imaging disc-shaped iron-nitride precipitate in the Fe-0.3Cu alloy (Ref. 29). As was discussed in the previous section, the bulk-irradiated iron alloys showed formation of nitride precipitates. The FIM/AP specimens were prepared from the

broken C_v specimens, and therefore the observation of iron-nitride is not surprising.

Frisius et al. (Ref. 32) have conducted SANS experiments on the same alloys as studied at the University of Florida. Their results indicate the existence of defects of ~ 15 Å in diameter with a number density of the order of 10^{17} cm^{-3} in the reference iron and the Fe-Ni alloy. However, the FIM/AP (Ref. 29) and the TEM studies did not reveal any clustering or void formation in these alloys. As will be discussed in Section 5, such a large number density of voids should give rise to significant strengthening, which has not bee observed in these alloys (Ref. 46).

3.2.2 Steel Alloys

Thin foil and extraction replica specimens of the irradiated steel alloys were examined using TEM for (1) the presence of irradiation-induced defects such as those found in the model iron, (2) the recovery of dislocation network alloys, and (3) evidences of irradiation-induced carbide microstructural changes.

The general microstructure appeared to be the same in irradiated steel alloys and similar to the unirradiated structure. Typical micrographs are presented in Fig. 19. Only a few sparsely distributed large dislocation loops were found in each of the steel alloys. Analysis of these loops suggested that they are interstitial loops of $b = a/2\langle 111\rangle$ type. Figure 20 shows the dislocation loops in the low P-low Cu (Code 67A) steel alloy. Detailed examination of a number of thin foils revealed that the high P and high Cu steel alloys contain fewer resolvable defects, and those that are resolvable were smaller than in the low P-low Cu steel. It should be noted that the high dislocation density of the steels makes it very difficult to single out very small defects.

No significant recovery in the dislocation substructure due to the neutron irradiation was observed. Compared to the iron alloys, the steel alloys contain much larger areas of sinks (lath boundaries, dislocation and carbide/matrix interfaces) for irradiation-induced point defects. As a result, the supersaturation of point defects is much lower in steel alloys, and only a very small number density of defect clusters are formed. The fact that no significant change in the substructure of the irradiated steel alloys was observed indicates that dislocations mainly act as neutral sinks.

In our third Interim Report (Ref. 23), we reported that no changes in the carbide structure due to irradiated were found. However, in more recent studies, fine precipitates were found in the high P-low Cu irradiated steel alloy, as shown in Fig. 21. Analysis of these precipitates showed that they are rod-like. Such precipitates were not found in the similar alloy in the unirradiated condition. Also, they were not found in the other irradiated steel alloys examined. Lott et al. (Ref. 47) have reported that in an A 302-B steel, with virtually identical composition and fluence level (~ x 10^{19} n/cm^2) as

Fig. 19 TEM micrographs showing the general microstructural features in the irradiated steel alloys. (a) Thin foil and (b) extraction replica. High-phosphorus low-copper (67C) alloy.

BEST COPY AVAILABLE

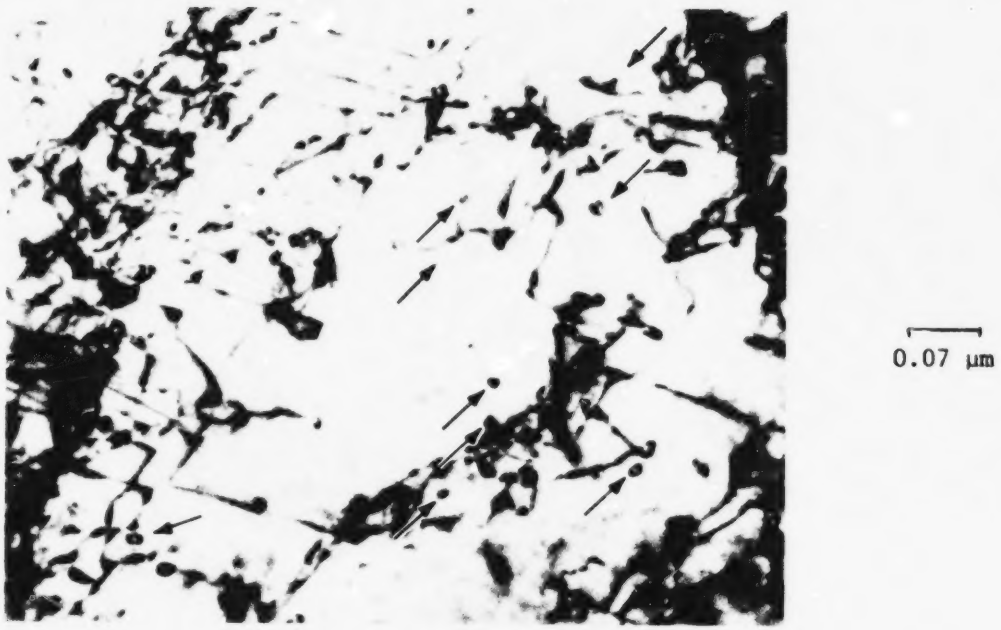

Fig. 20 TEM micrograph showing the sparsely distributed large dislocation loops in irradiated steel alloys. The loops are marked by arrows.

BEST COPY AVAILABLE

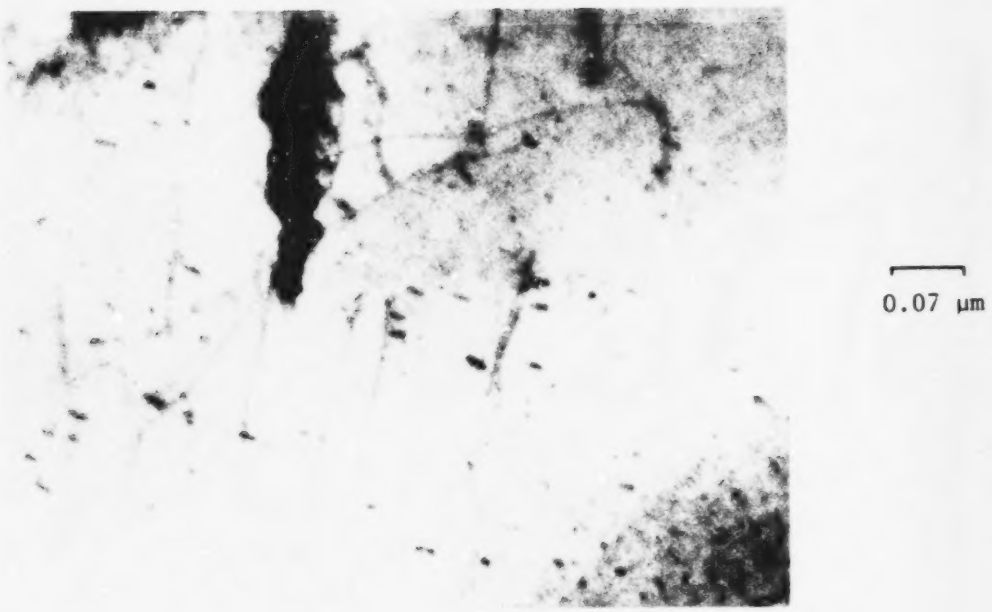

Fig. 21 TEM micrograph showing the fine needle-like precipitates found in the irradiated high P-low Cu steel alloy.

BEST COPY AVAILABLE

steels examined in this study, the Mo_2C carbides partially dissolve during irradiation and reprecipitate as fine (<200 Å) rods. Our analysis revealed that the needle-like precipitates observed in the high P-low Cu steel did not lie parallel to $\langle 100 \rangle_\alpha$ directions. This observation may suggest that they are not Mo_2C carbides. Buswell (Ref. 48) did not find any modification of the carbide microstructure in a study of a similar material irradiated to a fluence of 1×10^{19} n/cm^2. Considering the severe inhomogeneity in the microstructure of steel alloys, the small volume of the material examined in a thin foil, and the fact that small Mo_2C carbides are invisible using certain reflections, makes it difficult to draw any conclusions with respect to the effects of irradiation and alloying/impurity additions on the dissolution and reprecipitation of carbides.

It was attempted to analyze the irradiated steel alloys using the FIM/AP technique. Unfortunately, the samples flashed in the very early stages of the analysis. Recently, SANS analysis on these steel alloys has been performed by Beaven et al. (Ref. 49). They have concluded that the SANS results derived from Guinier plots could indicate that in low Cu-low P material (Code 67A), voids had formed during irradiation ($N \cong 5 \times 10^{16}$ n/cm^{-3}, $\bar{R} \cong 16$ Å). Due to the difficulties involved in TEM analysis of steel alloys, we cannot confirm such a finding. However, as will be discussed later, the small change in tensile properties due to irradiation suggests that the presence of such a high density of voids may not be realistic.

Beaven et al. (Ref. 49) have reported that in the presence of phosphorus (Code 67C alloy), a precipitate (or cluster) component appears in their SANS results. This finding is consistent with FIM/AP results, which indicate that phosphorus clusters in the absence of Cu for the low Cu iron alloy (Fe-Ni-P). The SANS results (Ref. 49) also indicate that Cu-rich precipitates had formed during irradiation. These precipitates are suggested to be rich in Mn and Ni. The enrichment of Cu clusters/precipitates with Ni has also been reported by FIM/AP results (Refs. 29, and 45).

3.3 Thermally Aged Iron Alloys

These alloys were thermally aged for ~ 1600 h at ~ 288°C to investigate the thermal contribution of irradiation at this temperature. Similar to the irradiated microstructure, thermal aging was found to dissolve ε-carbides and to cause precipitation of cementite. Eventually, the cementite particles had dissolved, and the grain boundary carbides had grown. The dissolution of cementite particles is demonstrated in Fig. 22, where the microstructure of the reference alloy, which had been heat treated at 288°C for only 20 min, is compared to a long-term thermally aged specimen.

The carbide dissolution seemed to be retarded in the phosphorus containing alloys, as demonstrated in Fig. 23. Phosphorus is a very surface active element and is known to segregate to carbide/matrix

Fig. 22 TEM micrographs showing the dissolution of cementite particles in the reference iron alloy after long time aging at 288°C. (a) Aged 20 min and (b) aged 1600 h.

BEST COPY AVAILABLE

(a)

0.7 μm

(b)

Fig. 23 TEM micrographs comparing the amount of cementite particles left in the matrix in (a) Fe-Ni-Cu alloy and (b) Fe-Ni-P alloy after thermal aging.

BEST COPY AVAILABLE

interfaces (Ref. 50). A reduction in the interface energy reduces the driving force for ripening, and hence the dissolution rate of in-matrix cementite particles is reduced. No significant effect of copper on the dissolution of carbides was found.

α"-nitrides were found on dislocations and on the cementite particles. Sets of micrographs showing the $g \cdot R = 0$ criterion for residual contrast for nitrides formed on dislocations and on carbides are presented in Figs. 24 and 25, respectively. α"-nitrides are known to precipitate on dislocations (Ref. 51); however, to the best of our knowledge, their nucleation on cementite has not been reported previously. In contrast to the irradiated iron alloys, in-matrix precipitation of α"-nitride was not observed in the thermally aged iron alloys. This observation suggests that either the thermally aged samples were cooled differently or, more possibly, the irradiation-induced solute-vacancy complexes enhance the in-matrix nucleation of α"-nitrides.

Since most of the nitrogen content of the iron alloys is soluble at ~ 288°C, we believe that α"-nitrides formed upon cooling from this temperature. Furthermore, very slow cooling rates are required to allow the precipitation of nitrides. This hypothesis was proven by heating two unirradiated wafer samples to 288°C and cooling one in the furnace and the other in the air. Figure 26 shows the formation of the α"-nitrides on a cementite particle in the former specimen and the absence of α"-nitrides in the latter. This experiment also confirms that the absence of nitrides in the wafer-irradiated samples is due to the faster cooling rate of these samples compared to the bulk-irradiated C_v specimens.

An interesting feature was observed in all thermally aged iron alloys examined. α"-nitrides were found on the periphery of the cementite particles that had already dissolved. Figure 27 shows the α"-nitride particles formed on the periphery of a cementite ghost which does not exist any longer. The micrographs in Fig. 27 should be compared to the micrographs presented in Fig. 26. As is apparent in Fig. 27b, the nitrides had nucleated on particles which are imaged differently than the nitride. Further analysis is required to identify these precipitates, which apparently had formed on the cementite/matrix interfaces and later, upon cooling from 288°C, had provided a nucleation site for α"-nitrides. Such cementite ghosts were not observed in the irradiated iron alloys, which suggests that no precipitation had occurred at the cementite/matrix interfaces.

The FIM/AP analysis was conducted on the thermally aged Fe-Cu alloy, and no copper clusters/precipitates were found (Ref. 29). In summary, the main differences between the thermally aged and the irradiated iron alloys are the presence of irradiation-induced (1) dislocation loops, (2) cluster/precipitates in copper- and phosphorus-containing alloys, and (3) complexes, possibly consisting of vacancy and alloying/impurity elements, and the absence of precipitates along the periphery of cementite ghosts in the irradiated alloys.

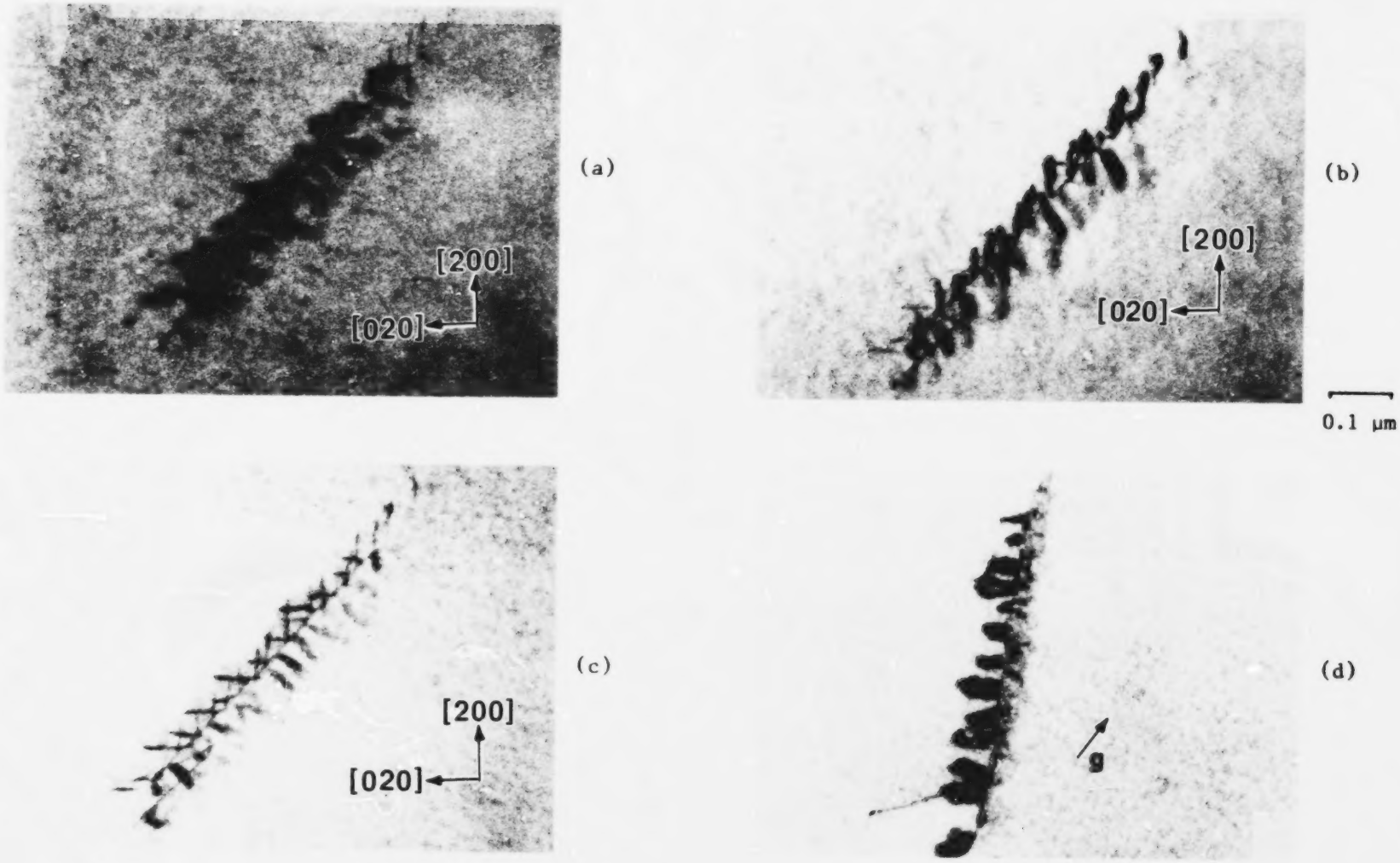

Fig. 24 TEM micrographs showing the image contrast of α''-nitrides formed on a dislocation line under dynamical two-beam condition. (a) B = [001], g = 200; (b) B = [001], g = 020; (c) B = [001], g = 110; (d) B = [111], g = $1\bar{1}0$.

BEST COPY AVAILABLE

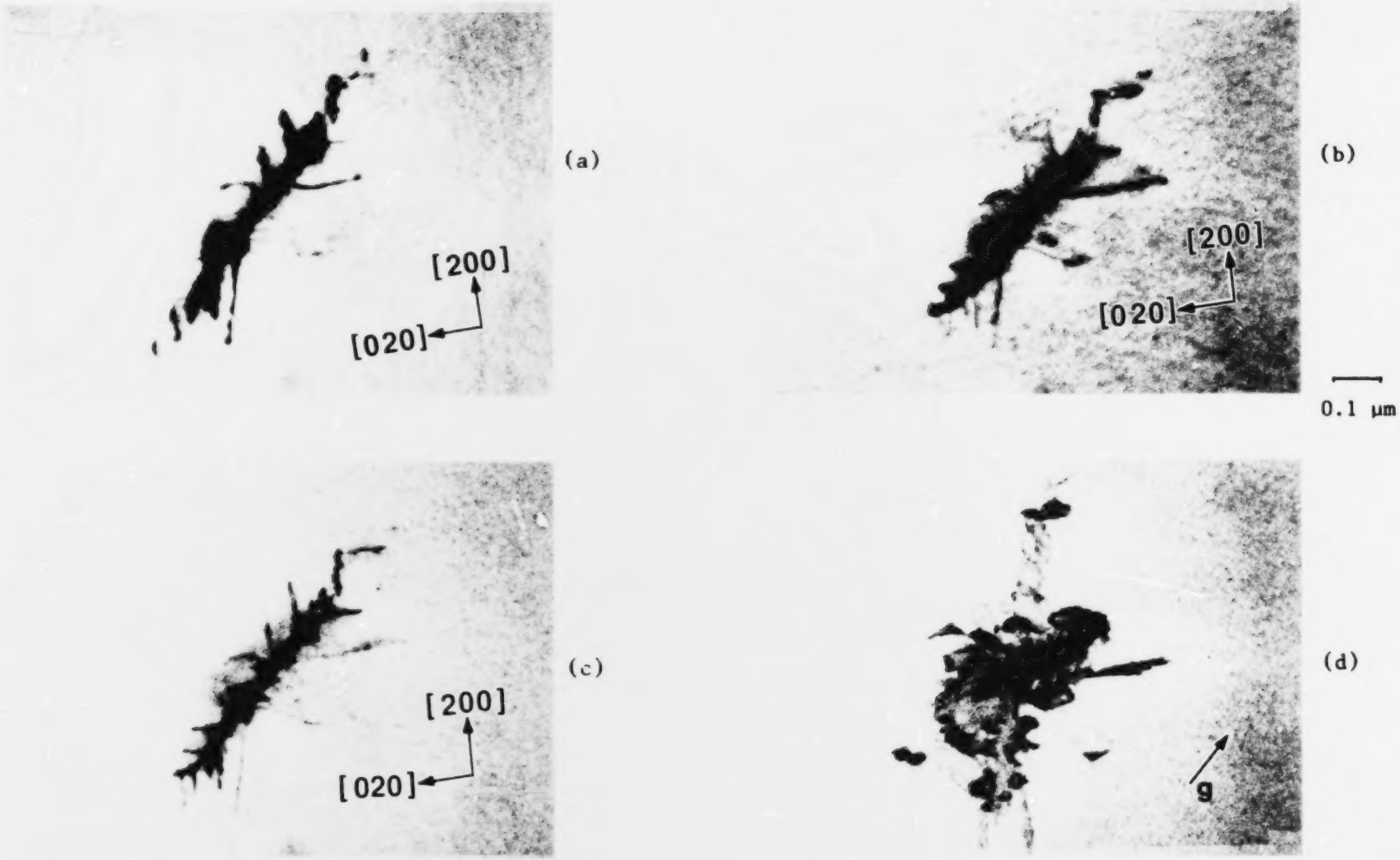

Fig. 25 TEM micrographs showing the image contrast of α"-nitrides formed on a cementite particle under dynamical two-beam condition. (a) B = [001], g = 200; (b) B = [001], g = 020; (c) B = [001], g = 110; (d) B = [111], g = $1\bar{1}0$.

BEST COPY AVAILABLE

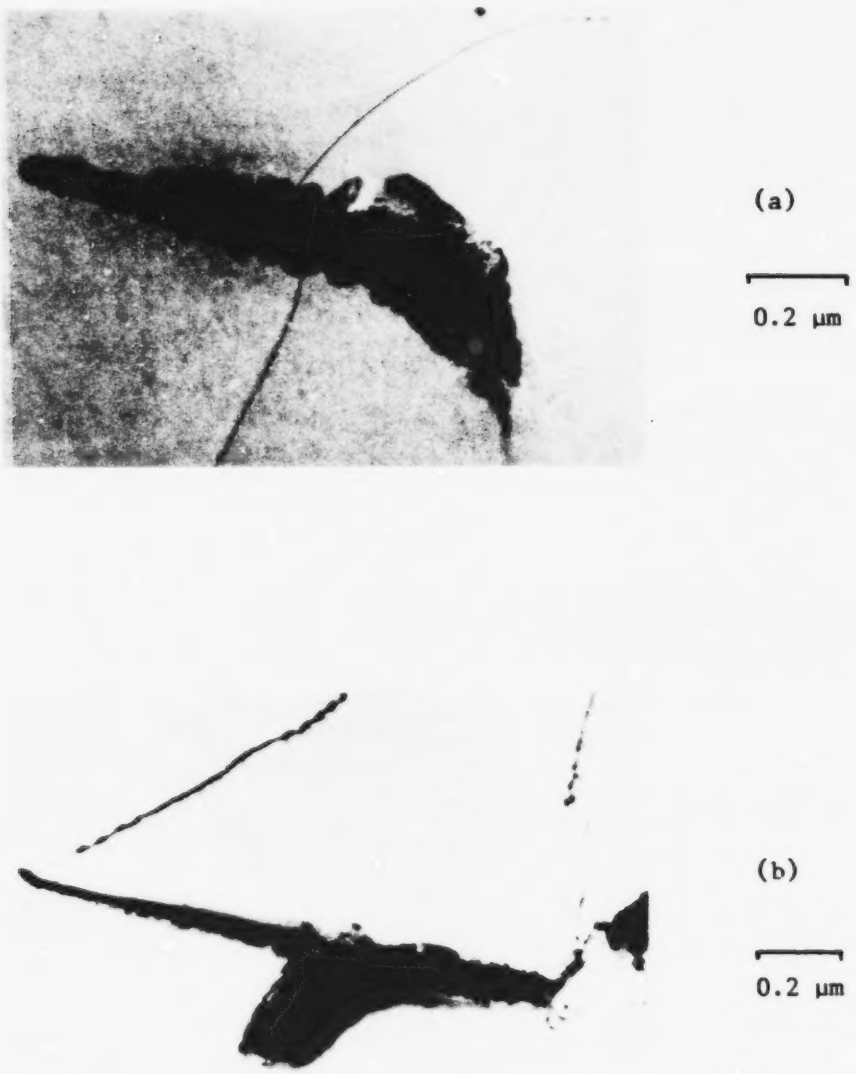

Fig. 26 TEM micrographs showing (a) the formation of α''-nitride on a cementite particle in a furnace-cooled iron alloy sample and (b) the absence of nitrides in an air-cooled iron alloy sample.

BEST COPY AVAILABLE

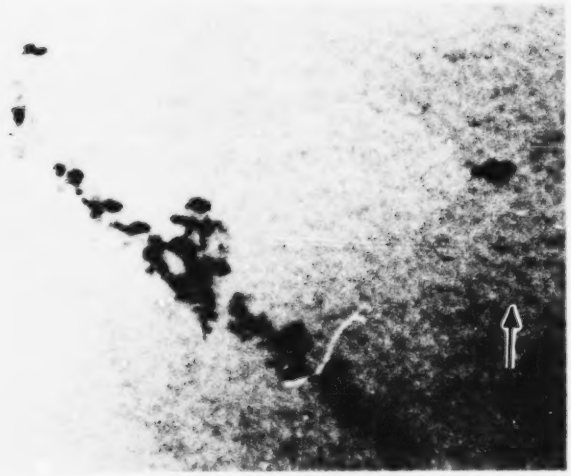

(a)

0.2 μm

(b)

Fig. 27 TEM micrographs showing the formation of α''-nitrides on precipitates formed on the periphery of a cementite ghost. (a) B = [011], g = 200; (b) B = [011], g = $0\bar{1}1$.

BEST COPY AVAILABLE

4. FRACTOGRAPHY AND THE FRACTURE SURFACE ANALYSIS

The fracture surfaces of selected broken C_v steel samples were studied in the irradiated and unirradiated conditions using SEM and AES/SAM with an emphasis on the effect of phosphorus. The possible mechanisms by which phosphorus could enhance the irradiation sensitivity of pressure vessel steels include (1) radiation-induced segregation to interfaces, (2) modification of possible radiation-induced changes in the carbide microstructure, (3) radiation-induced clustering/precipitation of phosphorus, and (4) modification of the defect aggregates. Mechanisms (1) and (2) would affect the fracture stress and/or strain, and the latter mechanisms would reduce the fracture toughness by increasing the yield strength and reducing ductility.

In general, the characteristics of ductile and brittle fracture surfaces were the same in the irradiated and unirradiated conditions. No intergranular fracture was found, and the brittle fracture was transgranular (cleavage), as shown in Fig. 28 for the high P-low Cu steel. Therefore, the promotion of intergranular fracture by grain boundary segregation of phosphorus was eliminated as a possible embrittlement mechanism.

It was interesting that the crack initiation mode was ductile in all the broken C_v specimens studied, even in samples with as low as 11 J (8 ft-lb) absorbed energy. The mode of crack initiation in fracture specimens is established by the shape of the ductile shear zone at the crack tip or notch root (Refs. 5 and 52). In the case of ductile initiation mode, the ductile shear zone has a thumbnail shape, as demonstrated by the fractographs given in Fig. 29.

Considering the ductile crack initiation mode and the fact that irradiation embrittlement is also manifested as a reduction in the upper-shelf energy, we pursued the subject of ductile cracking in the pressure vessel steels. The sizes of microvoids present on the fracture surface of steel alloys fell into three distinct size ranges. The extraction replicas from the ductile fracture surfaces showed that the very large microvoids (5-10 μm) were associated with MnS particles, the medium (2-5 μm) and small (< 2 μm) microvoids were associated with semispherical carbide and sometimes oxide or nitride precipitates. Most of the fracture surface was characterized by microvoids in the 1-μm size class, which are shown in Fig. 30. A quantitative analysis of the microvoid size distribution showed no effect of irradiation (Refs. 21 and 23). Therefore, it was concluded that no significant changes in the size distribution of carbides that participate in the ductile fracture had occurred upon irradiation.

The AES/SAM analysis of the ductile fracture surfaces of high P-low Cu specimens broken in-situ showed phosphorus accumulation at particle/matrix interfaces in both irradiated and unirradiated specimens. The particles analyzed were mainly inclusions, and the carbides found on the fracture surface were too small for analysis. Figures 31 and 32 show typical Auger spectra obtained for unirradiated and irradiated high P-low Cu steel. Qualitatively, for the irradiated specimen, a larger fraction of particles analyzed showed phosphorus

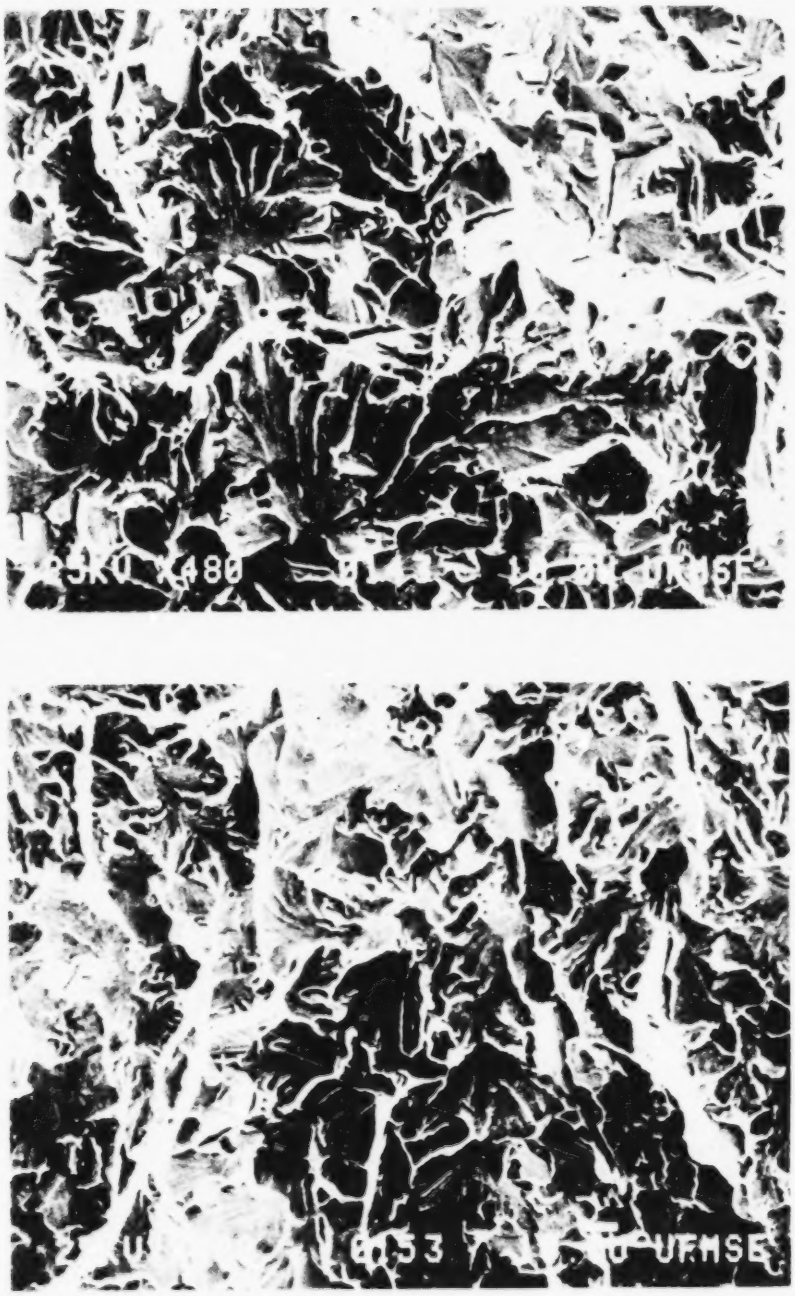

(a)

20 μm

(b)

Fig. 28 SEM fractographs showing the transgranular cleavage morphology of brittle fracture in (a) unirradiated and (b) irradiated high P-low Cu steel alloy.

BEST COPY AVAILABLE

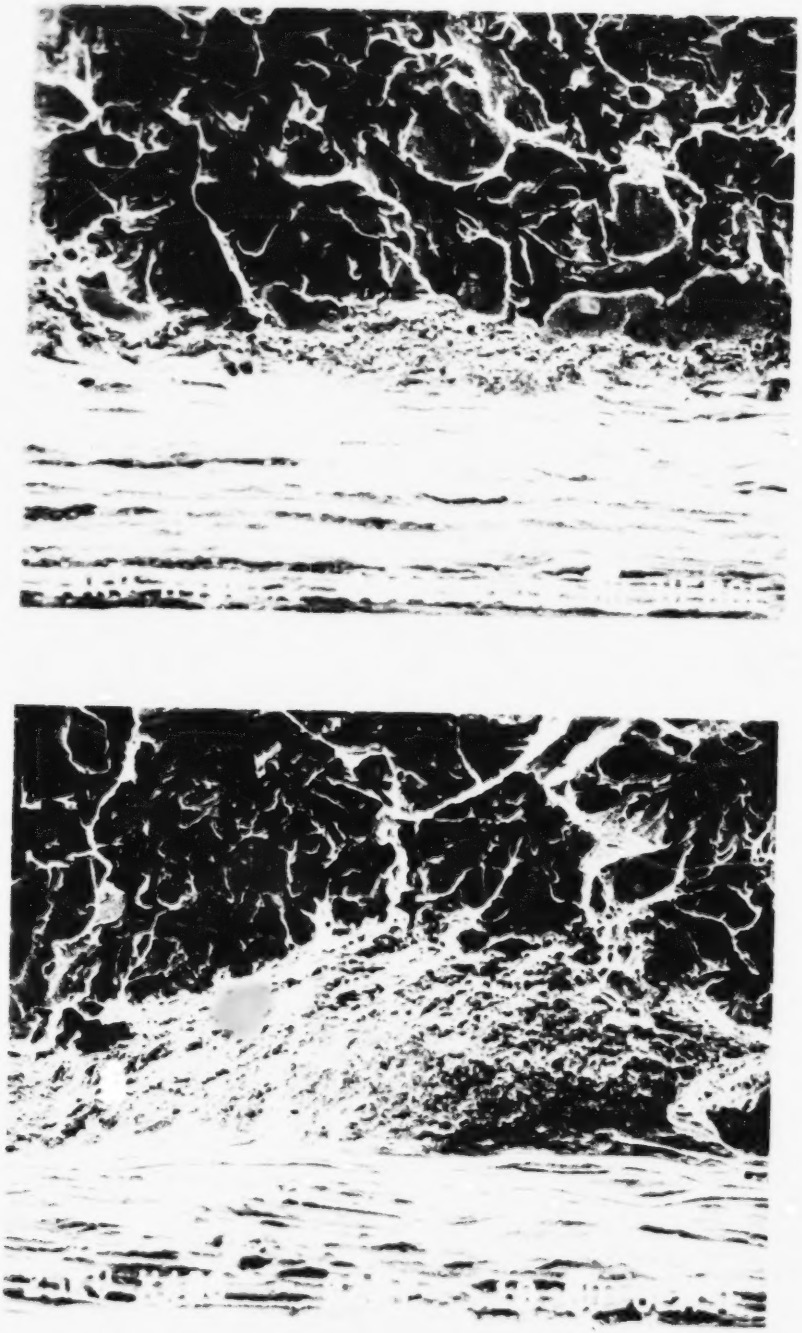

Fig. 29 SEM fractographs showing the shear zone adjacent to the V-notch in irradiated high P-low Cu steel fractured at -1°C with 11 J (8 ft-lb) absorbed energy at (a) the edge of the specimen and (b) the midthickness. Note the larger shear zone size at midthickness compared to the edge.

BEST COPY AVAILABLE

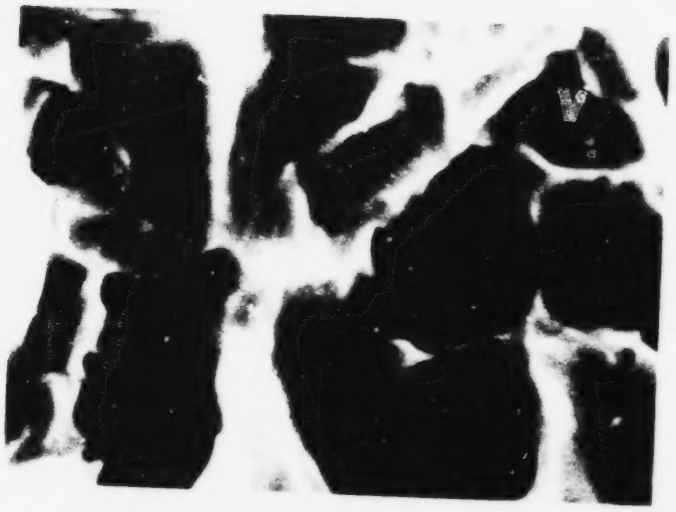

(a)

1 μm

(b)

Fig. 30 (a) SEM fractograph and (b) extraction replica TEM micrograph from the ductile fracture surface of an irradiated steel specimen.

BEST COPY AVAILABLE

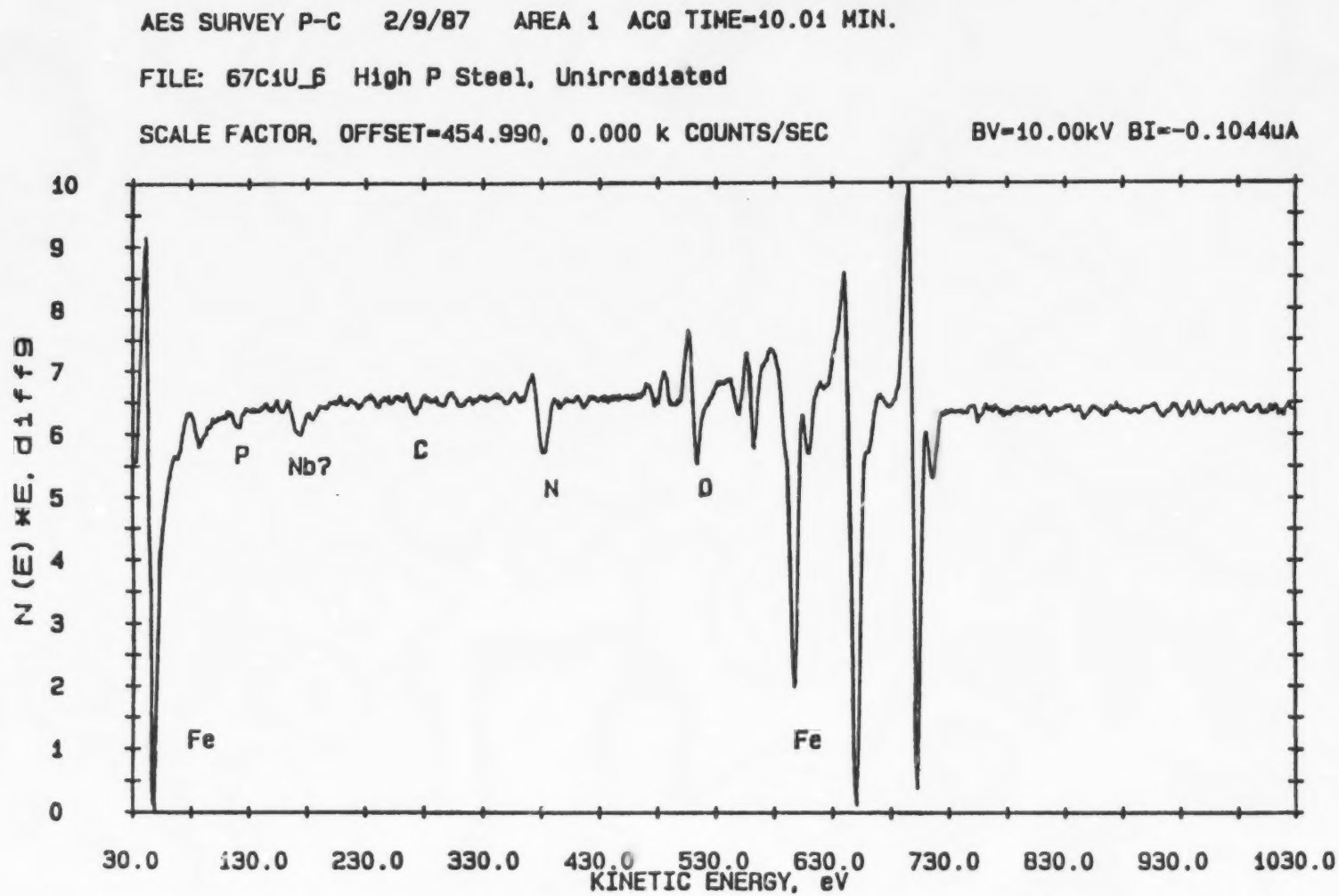

Fig. 31 Auger spectrum from the surface of a particle (Nb(C,N) + oxide?) showing phosphorus accumulation at the interface. Unirradiated high P-low Cu steel (67C).

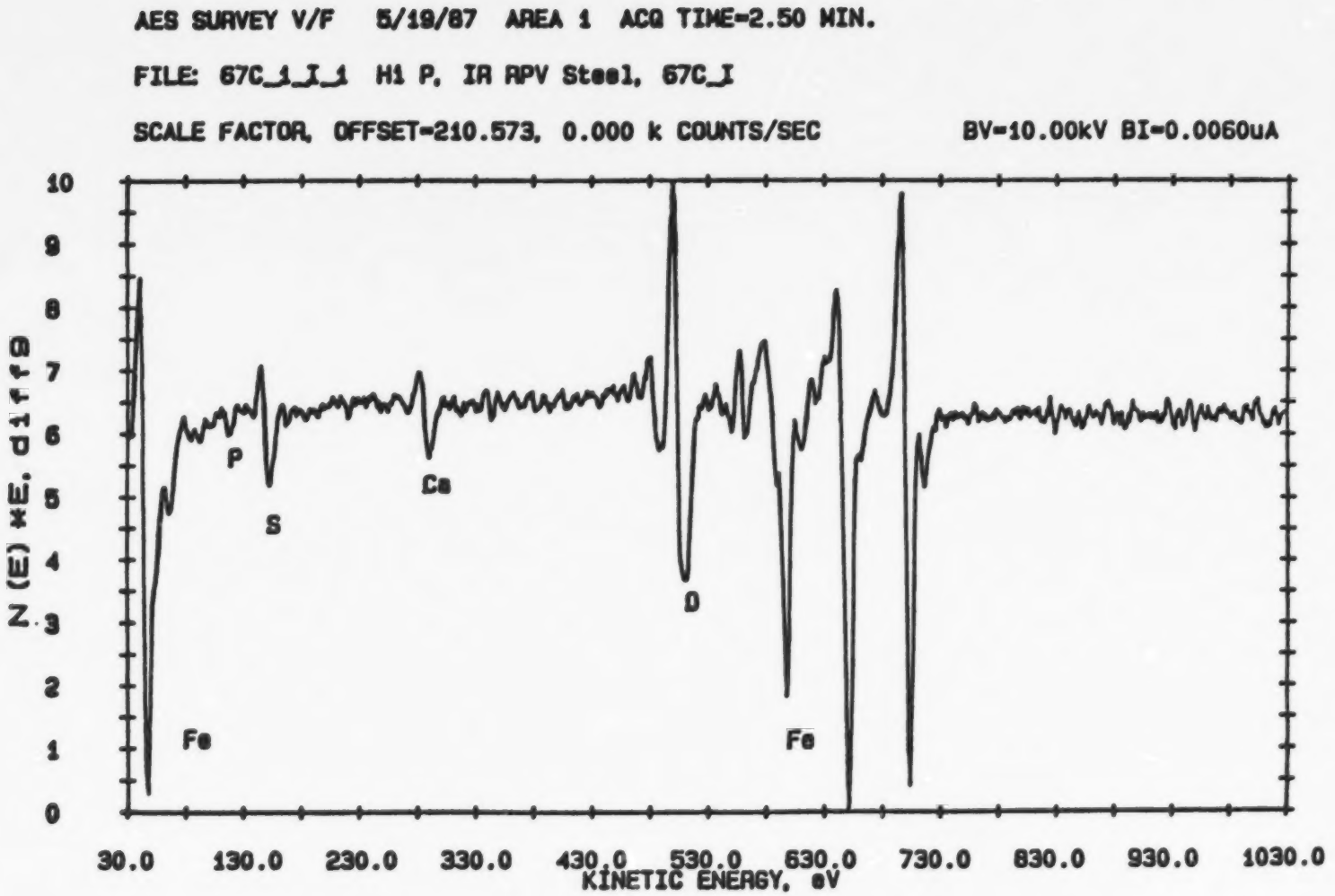

Fig. 32a Auger spectrum showing the accumulation of phosphorus on the surface of an oxide particle shown in Fig. 32b. Irradiated high P-low Cu steel (67C).

53

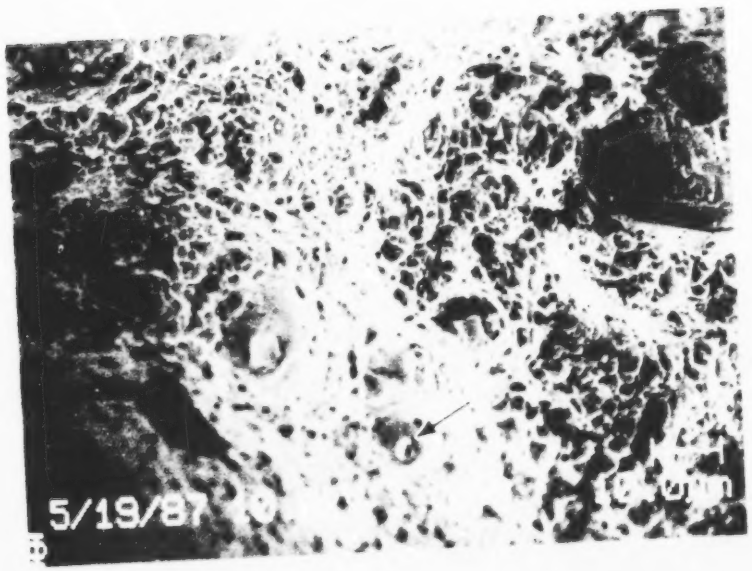

Fig. 32b - SEM micrograph showing the particle analyzed in Fig. 32a.

BEST COPY AVAILABLE

segregation compared to the unirradiated specimen. Since phosphorus segregation is usually inhomogeneous and localized (Ref. 50), it is difficult to draw any conclusions with regard to the irradiation-enhanced segregation of phosphorus to particle/matrix interfaces. However, as will be discussed later, the effect of phosphorus segregation is manifested as an equal reduction in the upper-shelf energy for irradiated and unirradiated C_v specimens. Therefore, it is concluded that phosphorus segregation causes embrittlement in both irradiated and unirradiated alloys. However, it is not the cause of enhanced irradiation embrittlement sensitivity of RPV steels.

5. THE CORRELATION BETWEEN MICROSTRUCTURE AND RADIATION HARDENING

The possible sources of hardening in the irradiated iron alloys are (1) dislocation loops, (2) clusters and precipitates, (3) voids, and (4) point defect-solute complexes. In general, the irradiation-induced aggregates impede the movement of glide dislocations. Therefore, a glide dislocation must be bent to some angle $0 < \phi < \pi$ before it can move on. For weak obstacles, as is the case for the above aggregates, using Fridel's statistics, the critical shear stress (τ_c) required to move a dislocation passed the obstacles of a random distribution is given by Reference 53:

$$\tau_c = \frac{2T}{bL}\left[\cos\left(\frac{\phi_c}{2}\right)\right]^{3/2} = \frac{2}{bLT^{1/2}}\left(\frac{F_c}{2}\right)^{3/2} \qquad (3)$$

where T = the glide dislocation line tension
b = Burgers vector
L = the mean distance between obstacles in the slip plane
ϕ_c = critical break-away angle
$F_c = 2T\cos\frac{\phi_c}{2}$ = critical break-away force acting on dislocation

In general, assuming $T \approx \frac{Gb^2}{2}$, the critical shear stress can be expressed as:

$$\tau_c = \alpha_c \frac{Gb}{L} \qquad (4)$$

where α_c is a function of ϕ_c (or F_c) and represents the strength of the obstacles and G is the shear modulus.

In the case of dislocation loops, $L = (2RN)^{-1/2}$ and:

$$\tau_L = \alpha_c\, GB\sqrt{2RN} \qquad (5)$$

Hirsch (Ref. 54) has reviewed the mechanisms of interaction of glide dislocations with point defect clusters such as dislocation loops in FCC crystals. His analysis shows that, depending on the deformation temperature and size of the loops, various mechanisms may be operative and α_c can vary from 0.8 (Orowan loop, $\phi_c = 0$) to as low as $\alpha_c = 0.05$ (long-range elastic interaction). Unfortunately, such analysis has not been done for BCC crystals. We have arbitrarily chosen α_c (b = 1/2<111>) = 0.3 for a theoretical prediction of strengthening in iron alloys due to dislocation loops. According to Eq. 3:

$$\alpha_c\ (b = \langle 100\rangle) = \left(\frac{b_{111}}{b_{100}}\right)^{3/2} \alpha_c\ (b = 1/2\langle 111\rangle) = 0.372 \qquad (6)$$

Russell and Brown (Ref. 55) have shown that for a random distribution of second phase particles as spheres of lower shear modulus than the matrix phase, such as coherent copper precipitates/clusters and voids, the shear stress is given by:

$$\tau = 0.8 \frac{Gb}{L}\left[1 - \left(\frac{E_1}{E_2}\right)^2\right]^{1/2}, \quad \sin^{-1}\frac{E_1}{E_2} \leq 50^\circ \tag{7a}$$

$$\tau = \frac{Gb}{L}\left[1 - \left(\frac{E_1}{E_2}\right)^2\right]^{3/4}, \quad \sin^{-1}\frac{E_1}{E_2} > 50^\circ \tag{7b}$$

$$\frac{E_1}{E_2} = \frac{E_1^\infty \log\frac{r}{r_o}}{E_2^\infty \log\frac{R}{r_o}} + \frac{\log\frac{R}{r}}{\log\frac{R}{r_o}} \tag{8}$$

where G = shear modulus of matrix
b = Burgers vector of glide dislocation

E_1^∞ = elastic modulus of matrix in an infinite body

E_2^∞ = elastic modulus of particle in an infinite body

r = particle diameter
R = outer cut-off radius $\approx 10^3 r_o$
r_o = inner cut-off radius $\approx 2.5b$
$L = \frac{f^{1/2}}{1.77r}$

f = volume fraction of particles

This model was proposed to explain the increase in yield strength and the lack of increase in strain-hardening rate due to the precipitation of Cu in the Fe-Cu system. For pure copper clusters, $E_1/E_2 = 0.6$ and for voids $E_1/E_2 = 0$. In both cases, at the limit of fine particles or voids ($r = r_o$), the energy of the dislocation in the particle or void becomes equal to the energy of the dislocation in the matrix and, therefore, there will be no strengthening.

When a distribution of obstacle strengths exists, as is the case in the irradiated iron alloys examined in this study, the total contribution of the obstacles to the yield strength can be approximated as (Ref. 53):

$$\tau^2 = \Sigma\tau_i^2 \tag{9}$$

The yield strength of a ferritic steel can be expressed as:

$$\sigma_y = \sigma_i + K_y d^{-1/2} \tag{10}$$

where σ_i = friction stress
d = grain size
K_y = a constant = f (T, ε, heat treatment)

The higher yield strength of the steel alloys in comparison to iron alloys is mainly due to boundary strengthening (bainitic lath boundaries), high dislocation density, and dispersion hardening by the smaller carbides. Assuming that irradiation-induced damage affect only the stress needed to move dislocations in the grains, i.e., friction stress, then the radiation hardening will be additive to Eq. 10 and can be expressed as:

$$\Delta\sigma_{irr} = 2.5\ Gb \left[\Sigma_i(\alpha_i/L_i)^2\right]^{1/2} \tag{11}$$

assuming $\sigma \simeq 2.5\tau$.

Tables 5 and 6 show the results of calculations for iron alloys and steel alloys, respectively, using the TEM results obtained in this study and SANS results reported by Frisius et al. (Ref. 32) and Beaven et al. (Ref. 49). As mentioned in previous sections, TEM and FIM/AP analyses did not reveal any void formation. In Table 5, a comparison of the calculated strength components with the measured radiation hardening reported by Hawthorne (Ref. 46) for the reference iron and the Fe-Ni alloy shows that the dislocation loops by themselves can account for the radiation hardening observed in these alloys and considering the voids will result in high strength levels. Furthermore, a consideration of the dislocation loops explains the decrease in radiation hardening due to the addition of nickel, which enhances formation of glissile b = a/2<111> loops. However, a consideration of voids predicts an enhanced radiation hardening due to the nickel addition. Similarly, as shown in Table 6, the SANS results suggest the formation of defect clusters in the low P-low Cu steel alloy (Code 67A), while the reported strength value (Ref. 20) reveals almost no radiation hardening in this alloy consistent with the very low dislocation loop density observed in this alloy.

In calculation of the radiation strengthening in the Fe-0.7Ni-0.025P alloy (Table 5), we have considered that the defect clusters detected by the SANS analysis (Ref. 32) are voids. However, on the basis of FIM/AP results (Ref. 29), we know that phosphorus clusters form

Table 5 Theoretical Predictions of Strengthening by Irradiation-Induced Aggregates in Iron Alloys

Alloy	Dislocation Loops (TEM)					Clusters/Voids (SANS)							$\Delta\sigma_{cal}$	$\Delta\sigma_{meas}$ [b]
								Voids		Cu-Rich Clusters				
	$\bar{d}$	N	L^{-1}	α	σ_L	$\bar{d}$ [a]	N [a]	L^{-1}	α	L^{-1}	α	$\sigma_{CL/V}$		
	(A)	(cm^{-3})	(A^{-1})		(MPa)	(A)	(cm^{-3})	(A^{-1})		(A^{-1})		(MPa)	(MPa)	(MPa)
Reference Iron	86	3.7×10^{15}	5.6×10^{-4}	0.366	101	14	1.7×10^{17}	1.27×10^{-3}	0.0897	———	———	58	116	103
Fe-0.3Cu	32	4.8×10^{15}	3.9×10^{-4}	0.355	71	41	6.1×10^{16}	———	———	1.28×10^{-3}	0.224	146	162	195
Fe-0.3Cu-0.7Ni	~12	$\sim 1.0 \times 10^{16}$	3.5×10^{-4}	0.3	54	41	6.9×10^{16}	———	———	1.34×10^{-3}	0.218	150	159	180
Fe-0.7Ni	28	6.5×10^{15}	4.3×10^{-4}	0.319	68	16	1.8×10^{17}	1.33×10^{-3}	0.1426	———	———	97	118	69
Fe-0.7Ni-0.025P	—	———	———	———	?	20	1.2×10^{17}	1.45×10^{-3}	0.235	———	———	175	175	146
Fe-0.7Ni-0.025P-0.3Cu	—	———	———	———	—	36	9.7×10^{16}	———	———	1.52×10^{-3}	0.2064	161	161	164

[a] Reference 32 [b] Reference 46

59

Table 6 Theoretical Predictions of Strengthening by Irradiation-Induced Aggregates in Steel Alloys

Alloy	Voids					Clusters/Precipitates					$\Delta\sigma_{meas}$
	$\bar{d}^a$ (A)	N^a (cm^{-3})	α	L^{-1} (A^{-1})	σ_V (MPa)	$\bar{d}^b$ (A)	N^b (cm^{-3})	α^c	d^{-1} (A^{-1})	σ_{CL} (MPa)	(MPa)
67A	16.	6.7×10^{16}	0.1535	8.35×10^{-4}	66	16.	4.9×10^{16}	0.2	7.06×10^{-4}	72	21
67B	15.4	6.9×10^{16}	0.1376	8.36×10^{-4}	59	15.4	1.8×10^{17}	0.2	1.33×10^{-3}	136	74
67C	19.	2.0×10^{16}	0.2147	4.9×10^{-4}	55	19.	7.5×10^{16}	0.2	1.03×10^{-3}	105	85
68A	22.	1.2×10^{17}	0.262	1.36×10^{-3}	182	22.8	6.6×10^{17}	0.1403	3.13×10^{-3}	225	232
68B	17.4	2.7×10^{17}	0.184	1.72×10^{-3}	162	19.6	1.0×10^{18}	0.1153	3.64×10^{-3}	215	260
68C	16.4	3.3×10^{17}	0.1621	1.86×10^{-3}	154	16.2	1.9×10^{18}	0.0859	4.35×10^{-3}	192	252

[a] Reference 49 [b] Reference 20 [c] We have arbitrarily assume $\alpha = 0.2$ for phosphorus clusters

during irradiation. The composition of these phosphorus-rich clusters and the mechanism of hardening by them are not known. However, the phosphorus addition clearly contributes to radiation hardening by radiation-induced clustering of phosphorus. The effect of phosphorus seems to be comparable in the iron alloys and the steel alloys. The addition of phosphorus increases the radiation hardening of the iron alloys by 77 MPa, from 69 MPa for the Fe-0.7Ni to 146 MPa for the Fe-0.7Ni-0.025P alloy. Similarly in the steel alloys, the radiation strengthening is enhanced by 64 MPa, from 21 MPa for the low P-low Cu alloy (Code 67A) to 85 MPa for the high P-low Cu alloy (Code 67C).

The addition of copper in the alloys studied contributes to radiation hardening mainly by irradiation-enhanced precipitation. In contrast to previously reported hypotheses (Refs. 9 and 13), copper does not contribute to irradiation hardening by modifying the irradiation-induced defect aggregates. Actually, as shown in Table 5 for iron alloys, the addition of copper results in a smaller contribution of dislocation loops to irradiation hardening.

The irradiation-induced increase in yield strength due to precipitation hardening, calculated on the basis of SANS data reported for the copper-containing alloys (Refs. 32 and 49), seems to be, in general, lower than the measured values reported for these alloys (Refs. 20 and 46) as shown in Tables 5 and 6. It should be noted that the calculated values are an upper limit due to the fact that copper clusters are not pure copper (Ref. 49). Consequently, the α value (Eq. 7), which depends on the modulus of the cluster, would be smaller if other elements such as Fe, Mn, or Ni are associated with the Cu-rich clusters. One other possible mechanism by which the addition of copper may enhance the irradiation hardening of iron and steel alloys is dislocation pinning by irradiation-induced segregation to dislocations. Such a mechanism would modify the K_y value in Eq. 10. However, there is not enough information available to evaluate this mechanism.

The steel alloys showed a larger enhancement in irradiation hardening by the addition of copper compared to the iron alloys. The addition of 0.3% Cu increased the irradiation hardening by 212 MPa in the steel alloys from 21 MPa for 67A alloy to 232 MPa for 68A alloy. However, the same amount of copper contributes to irradiation hardening by 92 MPa in the iron alloys from 103 MPa in the reference iron to 195 MPa in the Fe-0.3Cu alloy. Part of this difference is accounted for by the fact that the contribution of dislocation loops to the strengthening of irradiated alloys is reduced in the Fe-0.3Cu alloy (see Table 5). Furthermore, the SANS results (Refs. 32 and 49) show an order of magnitude higher number density of smaller Cu-rich precipitates in the 68A steel alloy compared to the Fe-0.3Cu iron alloy. This difference also contributes to the enhanced effect of copper on radiation hardening in the steel alloys.

The addition of phosphorus to copper-containing alloys did not enhance the irradiation hardening, as can be seen in Tables 5 and 6. This result is consistent with the FIM/AP findings (Ref. 29) that phosphorus does not cluster in the presence of copper in iron alloys.

6. COMMENTS ON RADIATION EMBRITTLEMENT OF RPV STEELS

The radiation embrittlement sensitivity of a reactor pressure vessel steel typically is evaluated by Charpy V-notch impact testing. C_v impact energy is one of the most complicated fracture toughness parameters in the sense it may include all of the processes of plastic deformation at high strain rates: crack initiation, crack propagation, crack arrest, reinitiation, and finally shear failure (Ref. 5). The material parameters that control these processes are: tensile stress-strain relationship (σ-ε), strain rate sensitivity, critical fracture stress (σ_f^*) and critical fracture strain (ε_f^*). The latter two parameters are usually controlled by microstructural features, in this case carbides and inclusions, of the order of > 0.1 μm, and the cohesive strength of interfaces. However, the σ-ε relationship is more sensitive to finer microstructural features.

Our analysis showed no significant changes in the carbide microstructure due to neutron irradiation. Phosphorus was found to be accumulated at particle/matrix interfaces in both unirradiated and irradiated high P steels. This is manifested as a higher ductile-to-brittle transition temperature and a lower upper-shelf energy of high P steels (Ref. 25). The microstructural changes caused by neutron irradiation (2.5 to 5×10^{19} n/cm^2, 288°C) in the iron and steel alloys examined were all at a fine scale and, as a result, they are expected to modify the stress-strain relationship. The tensile results reported by Hawthorne (Refs. 20, 25, and 46) indicate that the irradiation damage is manifested as an increase in the yield strength and a loss in the strain-hardening capacity†. As shown in the Appendix, although there is a correlation between the increase in yield strength and the shift in the ductile-to-brittle transition temperature or the reduction in upper-shelf energy, the scatter in data is significant. Probably a more appropriate factor for such empirical correlations would be the area under the true stress-strain curve.

The SEM analysis of fracture surfaces of C_v specimens revealed that the mode of crack initiation had been ductile in specimens with absorbed energy as low as 11 J (8 ft-lb). We suggest that the radiation embrittlement as evaluated by C_v impact testing is mainly associated with the loss in strain-hardening capacity, which causes shear localization near the notch tip. It should be realized that the reduction in strain-hardening capacity is the result of an increase in yield strength.

---

†The loss in strain-hardening capacity was evaluated by the analysis of stress-strain curves for iron alloys. The true maximum uniform strain was decreased from ~ 25% in unirradiated iron alloys to ~ 10% in the irradiated iron alloys. The strain-hardening rate in irradiated alloys was found to be minimum in the reference and highest in the phosphorus-containing alloys.

7. SUMMARY

This report summarizes the results of a three-year research program undertaken in the Department of Materials Science and Engineering at the University of Florida to investigate the mechanisms by which copper, phosphorus, and nickel modify the evoluation of microstructure in pressure vessel steels and model iron alloys upon exposures to fast neutrons. A series of pressure vessel steels and model iron alloys with various contents of copper, nickel, and phosphorus in unirradiated and irradiated conditions were provided by Materials Engineering Associates, Inc. The microstructures of these alloys were characterized using high resolution analytical microscopy techniques. A model is proposed to account for the effect of alloying/impurity elements on the evolution of dislocation loops in iron alloys. Existing strengthening models were reviewed. The microstructural findings of this study were combined with results of other studies (Refs. 20, 25, 29, 32, 46, and 49), and attempts were made to predict the radiation hardening of the examined alloys.

The results of our analyses can be summarized as follows:

- Neutron irradiation (fluence of 4.63×10^{19} n/cm^2, E > 1 MeV, 288°C) produced observable defects in all the model iron alloys examined. The analysis of the larger defects revealed they are prismatic dislocation loops of an interstitial nature with a<100> and a/2<111> Burgers vectors. Compared to the model iron alloys, the steel alloys showed a much lower number density of dislocation loops. The loops were larger and those analyzed had a/2<111>-type Burgers vectors. These differences are attributed to the large number of point-defect sinks in the steel alloys.

- Additions of copper, nickel, and/or phosphorus reduced the size, increased the apparent number density of observable defects and increased the fraction of a/2<111> dislocation loops. Following Little et al. (Ref. 35) these effects were explained by point-defect trapping by solute atoms, which results in a slower growth rate of a<100> loops and consequently a higher survival rate of a/2<111> loops. In contrast to reported SANS results (Ref. 32), voids were not found in the alloys examined.

- ε-carbides were observed in the matrix and on the dislocations in the unirradiated model iron alloys. Copper enhanced the in-matrix precipitation of ε-carbides significantly. The carbide microstructure was the same for the irradiated and thermally aged iron alloys. Cementite particles formed in the matrix within a short time on exposure to 288°C. Eventually, the grain boundary carbides grew at the expense of the in-matrix cementite particles by dissolution. Phosphorus seems to retard the dissolution process.

- The carbide and defect structures were the same in the wafer- and bulk-irradiated iron alloys. However, the bulk-irradiated samples but not the wafer-irradiated samples showed α"-nitride precipitates on dislocations, in the matrix and on the cementite

particles. The absence of nitride precipitation in the water-irradiated samples is attributed to the faster cooling rate of these specimens after the 288°C irradiation.

- We did not find a significant modification of the carbide microstructure of the steel alloys by neutron irradiation. Consistently, the size distributions of microvoids on the ductile fracture surfaces of the unirradiated and irradiated alloys were similar; the alloying/impurity content did not modify the distributions.

- Phosphorus accumulation was detected at particle/matrix interfaces in both unirradiated and irradiated high P steels. This segregation of P is responsible for the slight embrittlement of high P alloys; however, it is not the cause of enhanced irradiation embrittlement sensitivity of RPV steels. The absence of intergranular fracture in high P steels eliminated radiation-induced segregation of phosphorus to prior austenite grain boundaries as an embrittlement mechanism.

- Consistent with other reported studies (Refs. 12-14), copper precipitation/clustering was found to be enhanced by neutron irradiation, probably due to an increased diffusion rate. Copper increases the irradiation sensitivity of pressure vessel steels by a precipitation hardening mechanism. The reduction in defect size by copper, in fact, reduces the contribution of dislocation loops to radiation hardening in the copper-containing alloys. It is suggested that, for the irradiation conditions of this study, Cu modifies the dislocation loop structure by changing the kinetics of defect evolution rather than by providing nucleation sites.

- The addition of nickel decreases the dislocation loop size significantly; the Burgers vectors of those loops analyzed were predominantly $a/2\langle 111\rangle$ type. The slightly lower radiation hardening observed in the Fe-0.7Ni alloy in comparison to the reference iron is attributed to this modification of dislocation loop structure. Nickel was found to be associated with the Cu-rich clusters; however, this association is not expected to modify radiation embrittlement sensitivity significantly. No other synergism between copper and nickel was found.

- In the absence of copper, irradiation-induced clustering of phosphorus occurs. These clusters act as obstacles to the motion of glide dislocations and hence increase the yield strength of irradiated high P alloys. In the presence of copper, phosphorus is associated with Cu-rich clusters/precipitates in model iron alloys but does not cluster by itself. This observation correlates with the insensitivity to phosphorus content of radiation hardening and radiation embrittlement found in C_v tests for high Cu alloys.

Although many investigations have been performed to characterize the microstructure of neutron irradiated ferritic iron alloys in an undeformed condition, only very few studies of the deformation mechanism have been conducted. The strengthening mechanisms presented in this report are speculative. Experimental studies of plastically deformed conditions are essential for reaching new levels of understanding of radiation embrittlement.

REFERENCES

1. J. R. Hawthorne and L. E. Steele, The Effects of Radiation on Structural Metals, ASTM STP 426, American Society for Testing and Materials, Phila., PA, 1967, pp. 534-572.

2. J. R. Hawthorne, Treatise on Materials Science and Technology: Embrittlement of Engineering Alloys, Vol. 25, C. L. Briant and S. K. Banerji, Eds., Academic Press, 1983, pp. 461-524.

3. J. R. Hawthorne, H. E. Watson, and F. J. Loss, Effects of Radiation on Materials: Tenth International Symposium, ASTM STP 725 American Society for Testing and Materials, Phila., PA, 1981, pp. 63-75.

4. G. E. Lucas, G. R. Odette, P. M. Lombrozo, and J. W. Scheckherd, Effects of Radiation on Materials: Twelfth International Symposium, ASTM STP 870, American Society for Testing and Materials, Phila., PA, 1985, pp. 900-930.

5. F. Zia-Ebrahimi and G. Krauss, Acta Met., Vol. 32, 1984, pp. 1767-1777.

6. E. A. Little, International Metals Review, Vol. 21, 1976, pp. 25-60.

7. R. E. Smallman, Modern Physical Metallurgy, 4th Edition, Butterworths, 1985, pp. 289-334.

8. F. A. Smidt, Jr. and H. E. Watson, Met. Trans., Vol. 3A, 1972, p. 2065.

9. F. A. Smidt, Jr. and J. A. Sprague, Effects of Radiation on Substructure and Mechanical Properties of Metals and Alloys, ASTM STP 529, American Society for Testing and Materials, Phila., PA, 1973, pp. 78-91.

10. S. S. Brenner, R. Wagner, and J. A. Spitznagel, Met. Trans., Vol. 9A, 1978, p. 1761.

11. D. K. Hulett and W. A. Jesser, "TEM Studies and Microhardness Testing of Irradiated Ferritic Steels," to be published.

12. M. K. Miller and S. S. Brenner, Res. Mechanica, Vol. 10, 1984, pp. 161-168.

13. R. Wagner, F. Frisius, R. Kampmann, and P. S. Beaven, in Dimensional Stability and Mechanical Behavior of Irradiated Metals and Alloys, Proc. BNES Conf., Vol. 1, 1983, p. 171.

14. R. Wagner, F. Frisius, R. Kampmann, and P. A. Beaven, "Defect Microstructure and Irradiation Strengthening in Fe-Cu Alloys and Cu Bearing Pressure Vessel Steels," in Proc. of ASTM Euratom Symposium on Reactor Dosimetry, 1984, p. 549.

15. G. R. Odette, Scripta Met., Vol. 17, 1983, pp. 1183-1188.

16. R. Bullough, in Dislocations and Properties of Real Materials, Institute of Metals, London, 1985, pp. 283-311.

17. E. A. Little, in Dimensional Stability and Mechanical Behavior of Irradiated Metals and Alloys, British Nuclear Energy Society, London, 1984.

18. J. R. Hawthorne, "Significance of Nickel and Copper Content to Radiation Sensitivity and Postirradiation Heat Treatment Recovery of Reactor Vessel Steels," USNRC Report NUREG/CR-2948, 1982.

19. T. J. Williams, A. G. Thomas, R. A. Berrisford, M. Austin, R. L. Squires, and J. H. Venables, Effects of Radiation on Materials: Eleventh International Symposium, ASTM STP 782, H. R. Brager and J. S. Perrin, Eds., American Society for Testing and Materials, Phila., PA, 1982, p. 343.

20. J. R. Hawthorne, "Tensile Strength Determinations for Laboratory-Melted A 533-B and A 302-B Steel," MEA-2138, Materials Engineering Associates, Lanham, MD, Jan. 1986.

21. F. Ebrahimi and J. Hren, "Development of a Mechanistic Understanding of Radiation Embrittlement in Reactor Pressure Vessel Steels," Interim Report No. 1, University of Florida, Gainesville, FL, Oct. 1985.

22. D. T. Hoelzer and F. Ebrahimi, "Development of Reference Properties: Iron Alloys Microstructure," Interim Report No. 2, University of Florida, Gainesville, FL, May 1986.

23. D. Venables, D. T. Hoelzer, and F. Ebrahimi, "Preliminary Model Development: Phosphorus Effect," Interim Report No. 3, University of Florida, Gainesville, FL, Oct. 1986.

24. F. Ebrahimi and D. T. Hoelzer, "Preliminary Model Development: Copper and Nickel Effects," Interim Report No. 4, University of Florida, Gainesville, FL, June 1987.

25. J. R. Hawthorne, "Exploratory Studies of Element Interactions and Composition Dependencies in Radiation Sensitivity Development, USNRC Report NUREG/CR-4437, Nov. 1985.

26. K. F. Hale and D. McLean, "J. of Iron and Steel Institute, 1963, p. 337.

27. P. Ferguson, U. Dahmen, and K. H. Westmacott, Scripta Met., Vol. 18, 1984, p. 57.

28. F. Ebrahimi, B. Hoover, and D. T. Hoelzer, "On the Effect of Cu on ε-Carbide Nucleation," submitted to Scripta Met.

29. M. K. Miller, D. T. Hoelzer, F. Ebrahimi, J. R. Hawthorne, and M. G. Burke, "Characterization of Irradiated Model Pressure Vessel Steels," submitted to J. de Physique.

30. L. L. Horton, "A Transmission Electron Microscope Study of Fusion Environment Radiation Damage in Iron and Iron-Chromium Alloys," ORNL Report TM-8302, Oak Ridge National Laboratory, Oak Ridge, TN, 1982.

31. D. S. Gelles, "Microstructural Examination of Irradiated Simple Ferritic Alloys," Proc. of Intl. Conf. on Neutron Irradiation Effects, 1981.

32. F. Frisius, R. Wagner, and P. A. Beaven, "SANS Analysis of Irradiated and Unirradiated Model Alloys," First Progress Report, GKSS Forschungszentrum Geestacht, 1987.

33. I. M. Robertson, Ph.D. Dissertation, University of Oxford, England, 1982.

34. B. L. Eyre and R. Bullough, Phil. Mag. A, Vol. 12, 1965, p. 31.

35. E. A. Little, R. Bullough, and M. H. Wood, Proc. R. Soc. Lond., Vol. A(372), 1980, pp. 565-579.

36. V. Irmer and M. Feller-Kniepmeir, Phil. Mag., Vol. 21, 1970, p. 819.

37. G. Salje and M. Feller-Kniepmeir, J. Appl. Phys., Vol. 48, 1977, p. 1833.

38. E. A. Little, J. Nuclear Materials, Vol. 87, 1979, pp. 11-24.

39. F. A. Garner and A. S. Kumar, "The Influence of Both Major and Minor Element Composition on Void Swelling in Simple Austenitic Steels," in Effects of Radiation on Materials: 13th Int'l Symposium, 1986, to be published.

40. R. J. Weiss, Proc. Phys. Soc., Vol. 82, 1963, p. 281.

41. A. Azarian and K. Kheloufi, J. of Nuclear Materials, Vol. 9, 1981, pp. 25-26.

42. A. S. Keh and W. C. Leslie, Precipitation From Iron Base Alloys, G. R. Speich, Ed., Gordon and Breach Science Publishers, New York, 1965.

43. S. R. Goodman, S. S. Brenner, and J. R. Low, Met. Trans., Vol. 4, 1973, p. 2363.

44. S. R. Goodman, S. S. Brenner, and J. R. Low, Met. Trans., Vol. 4, 1973, p. 2371.

45. G. M. Worall, J. T. Buswell, C. A. English, M. G. Hetherinton, and G. D. W. Smith, J. of Nuclear Materials, Vol. 148, 1987, pp. 107-114.

46. "Structural Integrity of Light Water Reactor Pressure Boundary Components: Monthly Report for July 1986," F. J. Loss, Ed., MEA-2174, Aug. 1986.

47. R. G. Lott, S. S. Brenner, M. K. Miller, and A. Woldenden, ANS Trans., Vol. 38, 1981, p. 303.

48. J. T. Buswell, in "Analysis of the Behavior of Advanced Reactor Pressure Vessel Steels Under Neutron Irradiation - The UK Programme", report to IAEA from UKAEA, 1983, p. 281.

49. P. A. Beaven, F. Frisius, R. Kampmann, R. Wagner, and J. R. Hawthorne, "SANS Investigation of A 533-B Steels Doped with Phosphorus," presented to IAEA Specialists' Meeting on Irradiation Embrittlement and Aging of Reactor Pressure Vessel Steels, Philadelphia, PA, May 27-29, 1987.

50. F. Zia-Ebrahimi, "A Study of Mechanisms of Tempered Martensite Embrittlement in Low-Alloy Medium-Carbon Steel," Ph.D. Thesis, Colorado School of Mines, 1982.

51. P. A. Beaven and E. P. Butler, Acta Met., Vol. 28, 1980, pp. 1349-1359.

52. F. Ebrahimi, "A Study of Crack Initiation in the Ductile-to-Brittle Transition Region of a Weld," in Fracture Mechanics, 18th Symposium ASTM STP 945, American Society for Testing and Materials, Phila., PA, 1987, pp. 555-580.

53. L. M. Brown and R. K. Ham, Strengthening Methods in Crystals, Kelly and Nicholson, Eds., Applied Science, London, 1971, p. 12.

54. P. B. Hirsch, Vacancies 76, R. E. Smallman and J. E. Harris, Eds., 1976, pp. 95-107.

55. K. C. Russell and L. M. Brown, Acta Met., Vol. 20, 1972, pp. 969-974.

APPENDIX A

Analysis of the Correlation Between Radiation Hardening and Embrittlement of Pressure Vessel Steels

ANALYSIS OF THE CORRELATION BETWEEN RADIATION HARDENING AND EMBRITTLEMENT OF PRESSURE VESSEL STEELS

A number of researchers have advanced the proposal that the embrittlement of reactor pressure vessel steels arises primarily as a consequence of radiation-induced hardening (Refs. A1-A3). It is proposed that irradiation increases the yield strength of the material while leaving the critical fracture stress largely unchanged. Experimental confirmation of this idea has been attempted with moderate success by several investigators (Refs. A2-A5). Most recently, Odette, Lombrozo, and Wullaert (Ref. A5) have analyzed the relationship between hardening and embrittlement in some detail. They propose that the increase in DBTT can be expressed as

$$\Delta T_d = C\,\Delta\sigma_{ys};\quad C = \frac{1}{\Delta\sigma_{ys}} \int_{\sigma_{ys}(T_d^o)}^{\sigma_{ys}(T_d^o) - \Delta\sigma_{ys}} \left(\frac{\Delta\sigma_{ys}}{dT}\right)^{-1} d\sigma_{ys} \qquad (A1)$$

where σ_{ys} as a function of temperature is the <u>dynamic</u> yield stress; i.e., it is the yield stress determined at the strain rates (approximately $10^2\ s^{-1}$) typical of Charpy impact tests. It should be noted that the constant, C, is simply the mean reciprocal slope of this curve taken over the desired temperature and yield strength interval. That is, it represents a linear approximation of σ_{ys} vs. T over a relatively narrow range. Odette et al. further assumed that the irradiation hardening, $\Delta\sigma_{ys}$, is not dependent on temperature or strain rate and thus may be determined from the usual static tensile tests at any convenient temperature. They also showed that, due to upper-shelf energy effects, the DBTT measured from instrumented Charpy tests on unirradiated specimens, T_d^o, corresponds approximately to the 10-J level, not the 41-J level which is commonly used. In summary then, Odette et al. used a master curve of the <u>dynamic</u> yield stress vs. temperature combined with static measurements of irradiation-induced hardening, $\Delta\sigma_{ys}$, and a knowledge of the unirradiated DBTT, T_d^o, to predict the change in DBTT, ΔT_d.

In this Appendix, we will show, in a more clear way, how it is possible to use static tensile data (σ_{ys} vs. temperature and $\Delta\sigma_{ys}$) in conjunction with the unirradiated DBTT to calculate the constant, C, directly. This value can then be compared with the value determined from an empirical correlation of ΔT vs. $\Delta\sigma_{ys}$.

We start by assuming a linear dependence of σ_{ys} (static) on temperature with the understanding that this approximation is valid only over relatively small temperature or yield strength intervals.

$$\sigma_{ys} = a + bT \qquad (A2)$$

Based on the work of Steichen and Williams (Ref. A6) and Buchar et al. (Ref. A7), we can write an expression for the strain rate dependence of the yield (or flow) stress which is valid over the strain range 10^{-5} to 10^{2} s^{-1}:

$$\sigma_{\dot{\varepsilon}} = \sigma_1 + \alpha_o \ln \frac{\dot{\varepsilon}}{\dot{\varepsilon}_1} \tag{A3}$$

where $\sigma_{\dot{\varepsilon}}$ is the yield stress at the strain rate, $\dot{\varepsilon}$, σ_1 is the yield stress at $\dot{\varepsilon}_1$, and α_o is the strain rate sensitivity factor that represents the slope of a semi-log plot of σ vs. $\dot{\varepsilon}$. Furthermore, we can incorporate temperature dependence into this equation by substituting Eq. A2 for σ_1, and assuming that the strain rate sensitivity parameter, α_o, varies linearly with temperature, at least over the temperature interval of interest.

$$\alpha_o(T) = c + dT \tag{A4}$$

Substitute Eq. A2 and Eq. A4 into Eq. A3:

$$\sigma_{\dot{\varepsilon}} = a + bT + (c + dT) \ln \frac{\dot{\varepsilon}}{\dot{\varepsilon}_1}$$

Rearranging gives:

$$\sigma_{\dot{\varepsilon}} = a + c \ln \frac{\dot{\varepsilon}}{\dot{\varepsilon}_1} + \left(b + d \ln \frac{\dot{\varepsilon}}{\dot{\varepsilon}_1}\right) T \tag{A5}$$

For the irradiated condition, we can write a similar equation:

$$\sigma'_{\dot{\varepsilon}} = a' + c' \ln \frac{\dot{\varepsilon}}{\dot{\varepsilon}_1} + \left(b' + d' \ln \frac{\dot{\varepsilon}}{\dot{\varepsilon}_1}\right) T \tag{A6}$$

where the primes indicate that the material is in the irradiated condition. We are now in a position to apply the critical fracture stress criterion:

$$K\sigma'(T') = \sigma_f^* = \sigma\,(T)\ K$$

or

$$\sigma'(T) = \sigma(T)$$

where T' and T are the DBTT's in the irradiated and unirradiated conditions, respectively, and where K is the plastic stress intensity factor at the notch tip. Applying this criterion and rearranging yields:

$$T'\left(b' + d' \ln \frac{\dot{\varepsilon}}{\dot{\varepsilon}_1}\right) - T\left(b + d \ln \frac{\dot{\varepsilon}}{\dot{\varepsilon}_1}\right) = a - a' + (c - c') \ln \frac{\dot{\varepsilon}}{\dot{\varepsilon}_1} \qquad \text{(A7)}$$

Experimentally, it is observed that irradiation displaces the yield stress curve by a constant amount, $\Delta\sigma_{ys}$, as determined from static tensile tests (Refs. A2, A4-A6). Thus, we can assume that:

$$b' = b$$

and

$$\Delta\sigma_{ys} = a' - a$$

Finally, based on the work of Steichen and Williams (Ref. A6), we can assume that α_o is unaffected by irradiation at temperatures greater than approximately 27°C (300°K). Thus:

$$d' = d$$

and

$$c' = c$$

Substituting these values into Eq. A7 and rearranging yields:

$$T' - T = \frac{\Delta\sigma_{ys}}{-\left(b + d \ln \frac{\dot{\varepsilon}}{\dot{\varepsilon}_1}\right)}$$

or

$$\Delta T = C\,\Delta\sigma_y \qquad \text{(A8-1)}$$

where

$$C = \frac{-1}{b + d \ln \frac{\dot{\varepsilon}}{\dot{\varepsilon}_1}} \qquad \text{(A8-2)}$$

Thus, we can calculate the change in DBTT, ΔT, due to irradiation from a knowledge of how the yield stress changes with temperature (b), strain rate (d), and irradiation ($\Delta\sigma_{ys}$).

Using Williams and Hunter (Ref. A8) yield stress vs. temperature data for unirradiated A 533-B Class 1 pressure vessel steel at $\dot{\varepsilon} = 6.7 \times 10^{-5}\ s^{-1}$, we calculate the mean slope in the temperature regime between -8°C to 146°C to be b = 0.310 MPa/°C (0.0450 ksi/°C). The parameter of α_o as a function of strain rate was derived from the data of Steichen and Williams (Ref. A6). In the temperature range 25°C to 300°C, we can appro imate both the unirradiated and irradiated data as a straight line with a common slope d = 0.032 MPa/°C (0.0046 ksi/°C). Finally, assuming a typical strain rate of $10^{-2}\ s^{-1}$ for Charpy impact testing in Eq. A8-1:

$$C = 1.3°C/MPa = 9.1°C/ksi \qquad \text{(A9)}$$

Figure A1 shows a plot of ΔT vs. $\Delta\sigma_{ys}$ for A 533-B or A 302-B type steels with varying amounts of alloying/residual elements, derived from the data of Hawthorne (Refs. A9 and A10). The average slope, $\Delta T/\Delta\sigma_{ys}$, of this data is 0.68 ± 0.13°C/MPa (4.7 ± 0.9°C/ksi) which is approximately half the value predicted from the tensile data analysis presented here. This value is only slightly higher than the value of 0.50 ± 0.2°C/MPa reported in an empirical correlation of ΔT vs. $\Delta\sigma_{ys}$ for plate and forgings in power reactor surveillance programs (Ref. A4).

The discrepancy between the calculated and empirical values of C could result from underestimating the strain rate dependence of the A 533-B Class 1 steel since C depends sensitively on the slope, d, of α_o vs. T. Nevertheless, the basic approach of the model appears to be valid since its prediction of a strong dependence of ΔT on $\Delta\sigma_{ys}$ is qualitatively correct.

The radiation embrittlement sensitivity is also manifested as a reduction in upper-shelf energy (USE). Figure A2 shows a plot of the USE vs. $\Delta\sigma_{ys}$ derived from the data of Hawthorne (Refs. A9 and A10). It is interesting to note that, in contrast to Fig. A1, the intercept of the plot is not equal to zero, i.e., the upper-shelf energy can be reduced without an increase in the yield strength. Furthermore, there is a large scatter associated with the ΔUSE vs. $\Delta\sigma_{ys}$ plot. Theoretically,

the upper-shelf energy should be correlated with the energy under the true stress-strain curve truncated at maximum uniform strain. Such information was not available for evaluation.

REFERENCES

A1. A. S. Tetelman and A. J. McEvily, Jr., Fracture of Structural Materials, J. Wiley and Sons, 1967, p. 475.

A2. M. S. Wechsler, R. G. Berggren, N. E. Hinkle, and J. Stelzman, Irradiation Effects in Structural Alloys for Thermal and Fast Reactors, ASTM STP 457, American Society for Testing and Materials, Phila., PA, 1969, p. 242.

A3. R. A. Wullaert, Impact Testing of Metals, ASTM STP 466, American Society for Testing and Materials, Phila., PA, 1970, p. 148.

A4. G. E. Lucas, G. R. Odette, P. M. Lombrozo, and W. Sheckherd, Effects of Radiation on Materials: Twelfth Int'l Symposium, ASTM STP 870, Vol. II, American Society for Testing and Materials, Phila., PA, 1984, pp. 900-930.

A5. G. R. Odette, P. M. Lombrozo, and R. A. Wullaert, Effects of Radiation on Materials: Twelfth Int'l Symposium, ASTM STP 870, Vol. 2, American Society for Testing and Materials, Phila., PA, 1984, pp. 840-862.

A6. J. M. Steichen and J. A. Williams, J. of Nuclear Matl., Vol. 57, 1975, p. 303.

A7. J. Buchar, Z. Bilek, and F. Dusek, Effect of Radiation on Materials: 11th Int'l Symposium, ASTM STP 782, American Society for Testing and Materials, Phila., PA, 1982, p. 55.

A8. J. A. Williams and C. W. Hunter, Effect of Radiation on Substructure and Mechanical Properties of Metals and Alloys, ASTM STP 529, American Society for Testing and Materials, Phila., PA, 1973, p. 5.

A9. J. R. Hawthorne, "Exploratory Studies of Element Interactions and Composition Dependencies in Radiation Sensitivity Development, USNRC Report NUREG/CR-4437, 1985.

A10. J. R. Hawthorne, "Tensile Strength Determination for Laboratory-Melted A 533-B and A 302-B Steels," MEA-2138, Materials Engineering Associates, Lanham, MD, 1986.

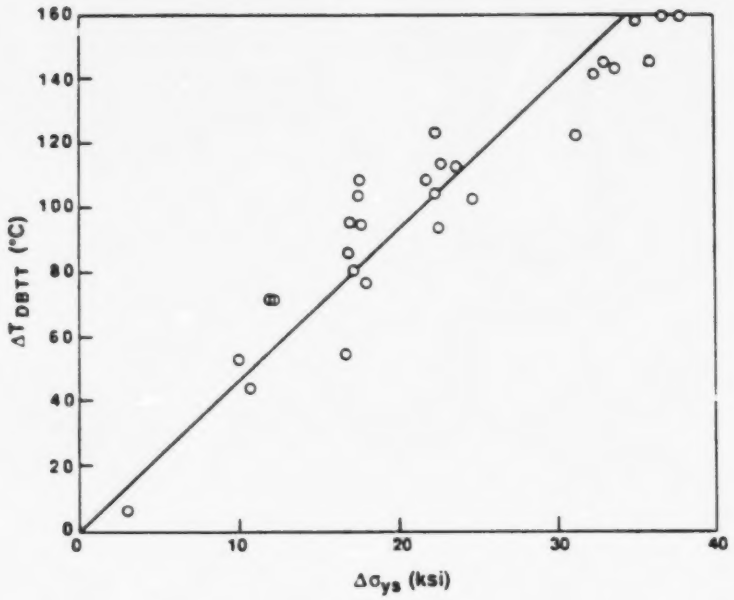

Fig. A1 Plot of the shift in ductile-to-brittle transition temperature, ΔT, vs. the increase in yield strength, $\Delta\sigma_{ys}$. Data from References A9 and A10.

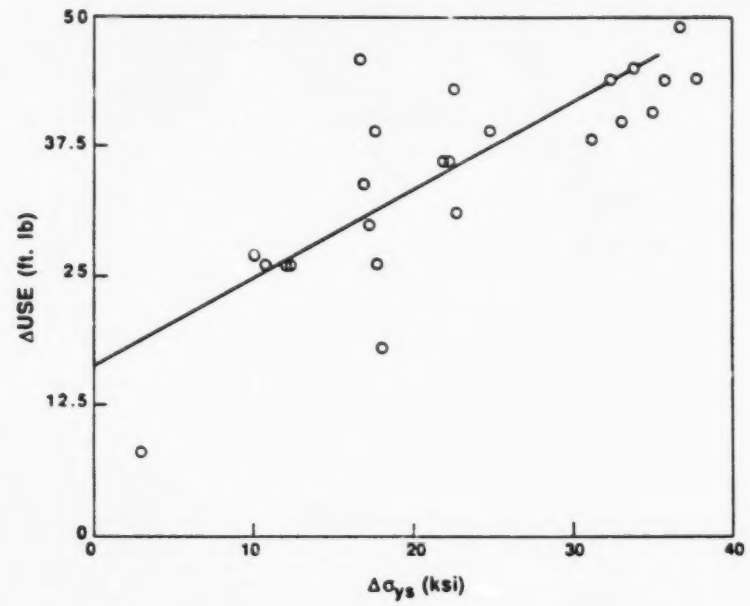

Fig. A2 Plot of the decrease in upper-shelf energy, ΔUSE, as a function of the increase in yield strength, $\Delta\sigma_{ys}$. Data from References A9 and A10.

BEST COPY AVAILABLE

NRC FORM 335 (11-81) U.S. NUCLEAR REGULATORY COMMISSION

BIBLIOGRAPHIC DATA SHEET

1. REPORT NUMBER (Assigned by DDC)
NUREG/CR-5063
MEA-2268

4. TITLE AND SUBTITLE (Add Volume No., if appropriate)
Development of a Mechanistic Understanding of Radiation Embrittlement in Reactor Pressure Vessel Steels
Final Report

2. (Leave blank)

3. RECIPIENT'S ACCESSION NO.

7. AUTHOR(S)
F. Ebranimi, D. T. Hoelzer, D. Venables, and V. Krishnamoorthy

5. DATE REPORT COMPLETED
MONTH: December YEAR: 1987

9. PERFORMING ORGANIZATION NAME AND MAILING ADDRESS (Include Zip Code)
Dept of Materials Science and Engineering
University of Florida Cainesville, FL 32611
Under contract to:
Materials Engineering Associates, Inc.
9700-B M. L. King, Jr. Highway Lanham, MD 20706-1837

DATE REPORT ISSUED
MONTH: January YEAR: 1988

6. (Leave blank)

8. (Leave blank)

12. SPONSORING ORGANIZATION NAME AND MAILING ADDRESS (Include Zip Code)
Division of Engineering
Office of Nuclear Regulatory Research
U. S. Nuclear Regulatory Commission
Washington, D.C. 20555

10. PROJECT/TASK/WORK UNIT NO

11. FIN NO
B8900

13. TYPE OF REPORT
Technical Report

PERIOD COVERED (Inclusive dates)

15. SUPPLEMENTARY NOTES

14. (Leave blank)

16. ABSTRACT (200 words or less)

The microstructures of a series of reactor pressure vessel (RPV) steels and model iron alloys with various Cu, Ni, and P contents were examined in unirradiated and neutron-irradiated conditions using high resolution analytical microscopy. Fractography techniques were also applied. Objectives were to isolate and identify the mechanisms by which these elements affect steel radiation embrittlement sensitivity as evidenced by notch ductility and tensile strength changes.

Radiation hardening of a reference iron alloy was found associated with the formation of prismatic dislocation loops of an interstitial nature. A very low density of loops was observed for a low Cu-low P steel having a low radiation sensitivity. Copper decreased the size and increased number density of observable defects; however, the enhancement of radiation sensitivity by Cu is due to a radiation-induced formation of Cu-rich clusters/precipitates. No synergism between Cu and Ni was found in the model iron alloys except for an enrichment of the Cu clusters with Ni. Alloys containing appreciable P did not show intergranular fracture. The detrimental effect of this impurity on radiation sensitivity for the case of a low Cu content is due to a radiation-induced clustering of P. Phosphorus clustering was found absent in a high Cu-high P iron alloy, consistent with the apparent inactive role of P in radiation sensitivity of high Cu steels. The effect of alloying/impurity elements on the evolution of defect structures during irradiation is ascribed to vacancy trapping by solute atoms, leading to an increased number density of defects.

17. KEY WORDS AND DOCUMENT ANALYSIS

17a. DESCRIPTORS

Radiation-Induced Precipitation
Radiation Effects Mechanisms
Irradiation Sensitivity
Impurity Element Effects
Electron Microscopy
Notch Ductility
Charpy V-Notch
Pressure Vessels
Nuclear Reactors
Embrittlement
A 302-B Steel
A 533-B Steel
Iron Alloys

17b. IDENTIFIERS/OPEN-ENDED TERMS

18. AVAILABILITY STATEMENT
Unlimited

19. SECURITY CLASS (This report)
Unclassified

21. NO OF PAGES

20. SECURITY CLASS (This page)
Unclassified

22. PRICE
$

NRC FORM 335 (11-81) *U.S. G.P.O. 1988-202-292/60334

BEST COPY AVAILABLE

UNITED STATES
NUCLEAR REGULATORY COMMISSION
WASHINGTON, D.C. 20555

OFFICIAL BUSINESS
PENALTY FOR PRIVATE USE, $300

SPECIAL FOURTH CLASS RATE
POSTAGE & FEES PAID
USNRC
PERMIT No. G-67

NUREG/CR-5069 DEVELOPMENT OF A MECHANISTIC UNDERSTANDING OF RADIATION EMBRITTLEMENT IN REACTOR PRESSURE VESSEL STEELS JANUARY 1988

BEST COPY AVAILABLE